Retrievals of cloud droplet size from the research scanning polarimeter data: Validation using in situ measurements

Mikhail D. Alexandrov[a,b,*], Brian Cairns[b], Kenneth Sinclair[c,b], Andrzej P. Wasilewski[d,b], Luke Ziemba[e], Ewan Crosbie[f,e], Richard Moore[e], John Hair[e], Amy Jo Scarino[f,e], Yongxiang Hu[e], Snorre Stamnes[e], Michael A. Shook[e], Gao Chen[e]

[a]*Department of Applied Physics and Applied Mathematics, Columbia University, 2880 Broadway, New York, NY 10025, USA*
[b]*NASA Goddard Institute for Space Studies, 2880 Broadway, New York, NY 10025, USA*
[c]*Department of Earth and Environmental Engineering, Columbia University, 2880 Broadway, New York, NY 10025, USA*
[d]*SciSpace, LLC, 2880 Broadway, New York, NY 10025, USA*
[e]*NASA Langley Research Center, Hampton, VA 23681, USA*
[f]*Science Systems and Applications, Inc., Hampton, VA 23666, USA*

Abstract

We present comparisons of cloud droplet size distributions (DSDs) retrieved from the Research Scanning Polarimeter (RSP) data with correlative *in situ* measurements made during the North Atlantic Aerosols and Marine Ecosystems Study (NAAMES). The airborne portion of this field experiment was based out of St. John's airport, Newfoundland, Canada with the focus of this paper being on the deployment in May - June 2016. RSP was onboard the NASA C-130 aircraft together with an array of *in situ* and other remote sensing instrumentation. The RSP is an along-track scanner measuring the polarized and total reflectance in 9 spectral channels. Its uniquely high an-

*Tel.: +1 212 678 5548; fax: +1 212 678 5552.
E-mail address: mda14@columbia.edu

gular resolution allows for characterization of liquid water droplet sizes using the rainbow structure observed in the polarized reflectance over the scattering angle range from 135 to 165 degrees. The rainbow is dominated by single scattering of light by cloud droplets, so its structure is characteristic specifically of the droplet sizes at cloud top (within unit optical depth into the cloud, equivalent to approximately 50 m). A parametric fitting algorithm applied to the polarized reflectance provides retrievals of the droplet effective radius and variance assuming a prescribed size distribution shape (gamma distribution). In addition to this, we use a non-parametric method, the Rainbow Fourier Transform (RFT), which allows us to retrieve the droplet size distribution itself. The latter is important in the case of clouds with complex microphysical structure, or multiple layers of cloud, which result in multi-modal DSDs. During NAAMES the aircraft performed a number of flight patterns specifically designed for comparisons between remote sensing retrievals and *in situ* measurements. These patterns consisted of two flight segments above the same straight ground track. One of these segments was flown above clouds allowing for remote sensing measurements, while the other was near the cloud top where cloud droplets were sampled. We compare the DSDs retrieved from the RSP data with *in situ* measurements made by the Cloud Droplet Probe (CDP). The comparisons generally show good agreement (better than 1 μm for effective radius and in most cases better than 0.02 for effective variance) with deviations explainable by the position of the aircraft within the cloud, or by the presence of additional cloud layers between the cloud being sampled by the *in situ* instrumentation and the altitude of the remote sensing segment. In the latter case, the multi-modal

DSDs retrieved from the RSP data were consistent with the multi-layer cloud structures observed in the correlative High Spectral Resolution Lidar (HSRL) profiles. The results of these comparisons provide a rare validation of polarimetric droplet size retrieval techniques, demonstrating their accuracy and robustness and the potential of satellite data of this kind on a global scale.
Keywords: Clouds, Electromagnetic scattering, Polarization, Rainbow, Remote sensing, *In situ* measurements

---

1. Introduction

Cloud feedbacks remain the most uncertain radiative feedbacks in climate models and there continue to be large uncertainties in the estimates of the forcings associated with aerosol-cloud interactions (e.g., Boucher et al., 2013; Flato et al., 2013). The optical properties of liquid water clouds depend on the droplet size distribution (DSD) while their radiative properties are controlled by their temperature (vertical location), water path and optical properties. In addition to providing data for understanding of cloud processes themselves, accurate and robust remote sensing estimates of droplet sizes for different cloud types (especially for broken clouds) are also crucial for studies of the interactions between clouds and aerosols.

In this study we focus on polarimetric techniques for cloud droplet size retrievals and estimate their accuracy by comparison with *in situ* measurements. Cloud droplet size retrievals from polarized observations of the reflected light in the rainbow region (at scattering angles between 135° and 165°) utilize the strong dependence of the polarized rainbow (cloud bow) on cloud DSD. The polarized rainbow structure is dominated by single scattering, thus, deriving the DSD or the parameters that define it from observations of the rainbow reduce, or eliminate, many of the uncertainties associated with 3D effects and unknown aerosol loadings. For the same reason, polarized rainbow observations carry information specific to the droplets at cloud top (within unit optical depth into the cloud) rather than weighted characteristics of the full cloud profile (as is the case for total reflectances, see e.g., Platnick (2000)). This is the same information that can be obtained from direct *in situ* measurements at cloud top which, can therefore be used for validation of remote sensing retrievals. The polarized rainbow technique has previously been used to retrieve cloud droplet effective radii from the Polarization and Directionality of the Earths Reflectances (POLDER, (Deschamps et al., 1994)) measurements (Bréon & Goloub, 1998; Bréon & Doutriaux-Boucher, 2005). A similar technique was adopted in the data analysis of the airborne Research Scanning Polarimeter (RSP) (Alexandrov et al., 2012b,a, 2015, 2016a) and was planned to be applied to satellite measurements from the Aerosol Polarimetery Sensor (APS) built as part of the NASA Glory Project (Mishchenko, 2006; Mishchenko et al., 2007). Unfortunately, despite extensive deployment of the RSP in numerous field experiments, until now, no direct validation of the polarized rainbow technique against *in situ* measurements has been possible. The purpose of this study is to fill this gap.

The North Atlantic Aerosols and Marine Ecosystems Study (NAAMES, https://naames.larc.nasa.gov/) is a five-year project focused on the lifecycle of the largest plankton bloom on Earth, which is in the North Atlantic, as well as on atmospheric aerosols and clouds. There are four combined ship and aircraft field deployments planned within the duration of the project.

Three of these deployments have already been completed. During these deployments the RSP, together with an array of *in situ* and other remote sensing instrumentation, was onboard the NASA Wallops Flight Facility C-130 research aircraft based at St. John's airport, Newfoundland, Canada. In this study we use the data from the second deployment (May 11 – June 5, 2016) when a series of patterns were flown that were specifically designed for comparison between remote sensing cloud retrievals and *in situ* measurements. Each of these patterns consisted of two flight segments with the same straight ground track. One of these segments was flown above clouds allowing for remote sensing measurements, while the other was inside the cloud where cloud droplets were sampled. The NASA Langley Research Center High Spectral Resolution Lidar (HSRL-1) deployed onboard the C-130 aircraft provided the cloud backscatter and depolarization profiles, which serve as the cloud vertical structure context for the RSP and *in situ* measurements. The airborne measurements made during NAAMES were complemented by satellite imagery and retrievals from NASA Geostationary Operational Environmental Satellite GOES-13 (operating as GOES-East) available at https://cloudsgate2.larc.nasa.gov/cgi-bin/site/showdoc?docid=22&lkdomain=Y&domain=NAAMES-SATGIF. These images provide synoptic-scale cloud system context for our intercomparison datasets.

2. The Research Scanning Polarimeter

2.1. Instrument design and measurements

The RSP (Cairns et al., 1999) is a scanning polarimeter, which scans its 14 mrad field of view in a meridional plane taking Earth viewing samples at 0.8° intervals within ±60° from the normal to the instrument base-plate, with additional observations of a polarimetric calibrator and a dark reference being obtained on the back side of each scan. The RSP has nine spectral bands centered at 410, 470, 550, 670, 865, 960, 1590, 1880, and 2260 nm. The wide angular and spectral ranges of the RSP measurements complemented by very high polarimetric accuracy ($< 0.2\%$ for the degree of polarization) and exceptional radiometric performance (stability of $\sim 1\%$/year) were among the reasons it was used as an airborne prototype for the satellite Aerosol Polarimetry Sensor (APS), which was built as part of the NASA Glory Project (Mishchenko, 2006; Mishchenko et al., 2007).

The RSP's design features three pairs of telescopes with one in each pair making simultaneous measurements of the linear polarization components of the intensity in orthogonal planes at 0° and 90° and the other making simultaneous measurements of linear polarization in orthogonal planes at 45° and 135°. The data obtained in each scan consists of 195 measurements of which ~ 150 are of the Earth scene, 10 are of the dark reference and 10 are of the in flight polarimetric calibrator. The intensity, and the degree and azimuth of linear polarization determined simultaneously from each of these measurements are then converted into the I, Q, and U components of the Stokes vector (Hansen & Travis, 1974; Mishchenko et al., 2006) and further into the total and polarized reflectances

$$R = \frac{\pi I}{\mu_s F_0} \quad \text{and} \quad R_p = -\frac{\pi Q}{\mu_s F_0}. \tag{1}$$

Here F_0 is the extraterrestrial solar irradiance and μ_s is the cosine of the solar zenith angle (SZA). The Stokes vector components, initially defined with respect to the scan plane of the instrument, are rotated (see Hansen & Travis, 1974) into the scattering plane (the plane containing both solar and view directions). There the contribution of first order scattering by spherical particles to Stokes parameter U is identically zero and higher order scattering contributions are negligibly small (Hansen & Travis, 1974; Mishchenko et al., 2006). This allows the polarized reflectance, R_p, to be related to a particular element of the phase matrix (Bréon & Doutriaux-Boucher, 2005). Note the difference between the sign convention used here (and also by Waquet et al. (2009); Alexandrov et al. (2012b,a, 2015, 2016a)) and that adopted by Bréon & Goloub (1998) and Bréon & Doutriaux-Boucher (2005).

The RSP makes measurements along the direction of travel of the aircraft and for the data analysis its actual scans are aggregated into "virtual" scans consisting of the reflectances at the full range of viewing angles at a single point on the ground or at cloud top (see, e.g., Alexandrov et al., 2012a).

2.2. Polarimetric retrievals of cloud properties

The polarimetric techniques for cloud droplet size characterization using the RSP data are based on analysis of the rainbow structure that is sharply defined in the polarized reflectance within the scattering angle range between 137° and 165° (Bréon & Goloub, 1998; Bréon & Doutriaux-Boucher, 2005;

Alexandrov et al., 2012b,a, 2015, 2016a). The structure of variations in the polarized reflectance in the angular range of the rainbow is dominated by single scattering of light by cloud particles, even though its amplitude can be affected by aerosols and the geometric structure of clouds. This fact allows us to avoid the retrieval uncertainties associated with 3D effects as well as unknown surface albedo, aerosol loadings, and amounts of ice over or mixed with liquid water layers. For the same reason the retrievals are accurate even for low cloud optical thicknesses (COTs), down to unity. The single-scattering nature of the rainbow structure makes the RSP retrievals representative of a unit effective optical depth into the cloud (Alexandrov et al., 2012a).

Two different methods for rainbow structure analysis were developed in our previous studies. Both of these methods are applied to RSP data in five visible and near infrared (NIR) bands: 410, 470, 550, 670, and 865 nm. The first method is a parametric technique (Alexandrov et al., 2012a), which fits the angular shape of the polarized rainbow from Eq. (1) using the functions of the form

$$R_p(\theta) = A \cdot P_{12}^{(Mie)}(\theta; r_{\text{eff}}, v_{\text{eff}}) + B \cdot \cos^2\theta + C, \tag{2}$$

where θ is the scattering angle, r_{eff} and v_{eff} are respectively the effective radius and variance of the cloud droplet size distribution (see Appendix A for definitions of DSD parameters). Phase matrix elements $P_{12}^{(Mie)}(\theta)$ forming a look-up table (LUT) are pre-computed according to Mie theory with 0.2° resolution in scattering angle. These computations assume that the droplet size distribution has a gamma distribution shape, thus, the parametric retrieval technique returns the effective radius and variance of such a DSD. The grid values of r_{eff} in this LUT range from 5 to 30 μm with 0.5 μm increments. The grid for v_{eff} runs from 0.002 to 0.35, with spacing depending on the value range (0.002 for $v_{\text{eff}} < 0.008$; 0.01 for $v_{\text{eff}} \in [0.008, 0.14]$; and 0.025 for $v_{\text{eff}} > 0.14$). The spacing of the tabulated values of effective variance is designed so that it is not a limiting factor in retrieval accuracy, but does reflect the increasing uncertainty in the retrieval of v_{eff} as a function of its value. The ranges for r_{eff} and v_{eff} have been sufficiently wide for all types of clouds that we have observed to this day. The coefficients A, B, and C in Eq. (2) are empirical fitting parameters accounting for contributions to the polarized reflectance from everything beyond single scattering by cloud droplets. These include multiple scattering, Rayleigh scattering by the atmosphere, aerosol and overlaying cirrus cloud extinction, ground surface reflectance for thin clouds, etc. Note that contributions of these factors to the polarized reflectance are slow functions of scattering angle easily separated by a regression from sharp rainbow structure.

The second method, the Rainbow Fourier Transform (RFT, (Alexandrov et al., 2012b)) retrieves the whole DSD without *a priori* assumptions of its functional shape. It is based on the observation that Mie-theory-derived polarized reflectance as a function of both the scattering angle (in the rainbow angular range) and the (mono-disperse) particle radius is akin to a kernel of an integral transform (similar to the sine Fourier transform on the positive semi-axis). The direct transform (with integration over radius) is simply the computation of the polarized reflectance for a given DSD, while the inverse transform (with integration over scattering angle) allows the DSD to be estimated from this polarized reflectance. The contributions of multiple scattering and other factors, beyond single scattering by cloud drops, described above are assumed to have the same effect on R_p as in Eq. (2) and are removed using a regression as a part of the RFT algorithm (see Section 7 in Alexandrov et al. (2012b) for details). The RFT is computationally faster than the parametric method, since it does not involve fitting of LUT.

The RSP's high angular resolution provides detailed characterization of the polarized rainbow, which translates into accurate determination of the DSD shape using the RFT. In the case of narrow monomodal DSDs, such as those observed at the top of shallow cumulus and stratocumulus clouds, both methods demonstrated an excellent agreement (Alexandrov et al., 2015). The situation is different in cases involving multilayer cloud systems such as fogs (Alexandrov et al., 2015) and high-altitude supercooled liquid water or mixed-phase clouds (Alexandrov et al., 2016a). In such cases the RFT allows us to retrieve multimodal DSDs with different size modes (each having gamma-distribution shape) that corresponding to the DSDs of different cloud layers. These modes can then be extracted and characterized separately (Alexandrov et al., 2015, 2016a). In contrast, such multimodality is only indicated in the parametric retrievals by a large v_{eff} of 0.1 or greater, which does not represent a local microphysical DSD (e.g., observable *in situ*). The advantage of the parametric fitting technique is in its better stability due to lower sensitivity to noise and artifacts in the measurements. It also can work on data with a more limited scattering angle range. The two retrieval methods usually complement and cross-validate one another, thus, in this study we present the results from both of them.

3. Comparison between remote sensing and in situ measurements

For comparison between remote sensing cloud retrievals and *in situ* measurements we use the data from specifically arranged pairs of flight segments sharing the same straight ground/cloud track: one above clouds allowing for remote sensing measurements, the other – inside the cloud where cloud droplets were sampled. The polarized cloud bow is generated over a unit optical depth from the cloud top (Alexandrov et al., 2012a), thus, we selected the parts of the *in situ* segments when the aircraft was either entering, or exiting the cloud or grazing its top. The dataset that we use for *in situ* validation of RSP droplet size retrievals was derived from Cloud Droplet Probe (CDP) measurements. This instrument was deployed on the same NASA C-130 aircraft as the RSP and was operated by the NASA Langley Aerosol Research Group Experiment (LARGE) group (https://science.larc.nasa.gov/large/).

The CDP (http://www.dropletmeasurement.com/products/airborne/CDP-2) is a low-power cloud particle spectrometer measuring droplets in the diameter range between 2 and 50 μm for concentrations as high as 2000 particles/cm^3 (Lance et al., 2010). The manufacturer-stated qualified sample cross section for the CDP is 0.24 mm^2. The swept volume is dependent on true airspeed, which during NAAMES in-cloud segments varied between 100 and 120 m/s. Generally, the CDP's counting rate can be affected by the "coincidence" artifact (Lance, 2012), when more than one droplet is detected at the same time, thus, resulting in the underestimation of the droplet number concentration and a high bias in the cloud particle size. However, this is unlikely to be an issue for the relatively large droplet sizes and low number concentrations encountered during NAAMES. It should be mentioned that

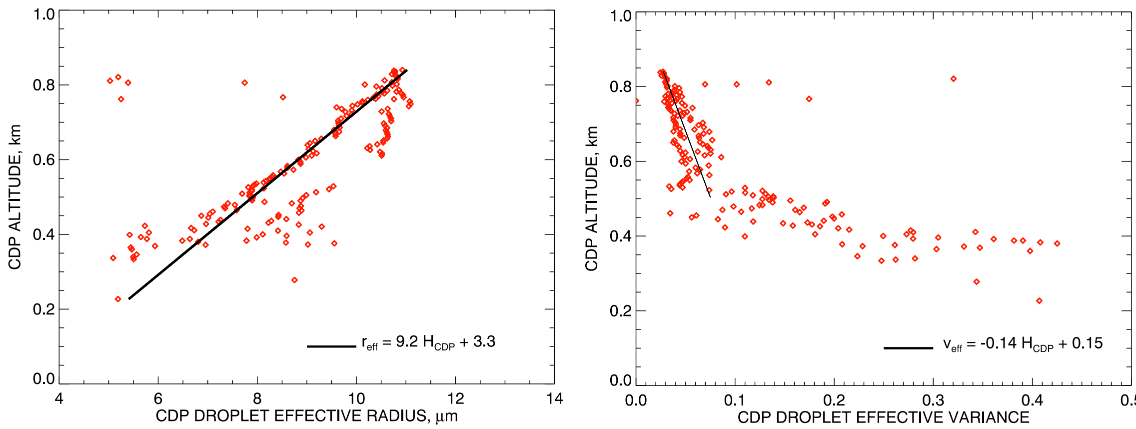

Figure 1: CDP-derived vertical profiles of droplet effective radius (left) and variance (right) for May 18, 2016 (see Fig. 3 for the location and CDP altitude). Linear fits are provided to show how fast these parameters change with altitude near cloud top.

the CDP has very small dead time losses and also uses fast electronics (40 MHz clock) which leads to major performance improvements of this instrument compared to its predecessors (Lance et al., 2010). The CDP sampling histograms are reported at 1 Hz rate, that makes each of them representative of a linear segment 100–120 m long (or volume of about 26 cm^3).

The RSP continuously scans 14 mrad field of view taking 0.8 sec for each scan. This field of view $\Delta\theta$ translates into horizontal footprint of the length

$$\Delta x = h\ (1 + \tan^2\theta)\ \Delta\theta, \tag{3}$$

where θ is the viewing angle and h is the aircraft altitude above cloud (cf. Alexandrov et al., 2016b). During NAAMES' remote sensing segments the C-130 aircraft typically flew at about 5000 m above cloud top with the speed $\sim$ 160 m/s. This corresponds to the length of a single-pixel footprint being 70 m (nadir view) at cloud top and the distance between centers of successive nadir footprints being 128 m. A unit optical depth from the cloud top, which contributes to RSP measurements, is achieved after 15 m, for droplets of 10 μm radius with a concentration of 100 drops per cm^3. However, strong forward scattering by cloud drops such as these means that the total depth that contributes to the cloud bow is about 50 m for this droplet size and concentration. The sampling volume for RSP is therefore very different to CDP ($\sim 10^{12}$ cm^3), but the horizontal scale for a single sample for both RSP and CDP is similar at $\sim$ 100 m.

Most of the clouds observed during the NAAMES deployments over the North Atlantic had DSD profiles where the effective radius increases and the effective variance decreases significantly with height as a result of condensational growth of droplets as cloudy air parcels are lifted (Rogers & Yau, 1989). An example of this behavior provided by CDP observations as a function of the aircraft altitude inside cloud is shown in Figure 1. This reveals rapid changes in both r_{eff} and v_{eff} with the depth into cloud and these changes are quantified in Fig. 1 using linear fits to observations of the upper part of the cloud. We see from Fig. 1 (left) that $\Delta r_{\text{eff}}/\Delta H_{CDP} \approx 10$ μm/km, meaning that the effective radius decreases by 1 μm for each 100 m of depth into the cloud. Similarly, Fig. 1 (right) shows that v_{eff} increases by more than 0.01 at a 100 m depth into cloud top. Thus, direct comparisons between RSP retrievals of DSDs and *in situ* measurements from CDP are only appropriate when the latter are made at cloud top.

We note that there are few data points at cloud top in Fig. 1 which sharply deviate from general profile, showing smaller r_{eff} (down to 5 μm) and larger v_{eff} (up to 0.3). These data are consistent with droplet evaporation due to cloud-top entrainment, and due to their small contribution to the RSP sampling volume do not show up in RSP retrievals. To avoid the influence of such data (as well as any noise in CDP measurements) in comparisons with RSP, we impose a certain smoothness condition on CDP data by removing data points deviating by more than 1 μm in r_{eff} from one of its immediate neighbors. Together with the requirement of $r_{\text{eff}} > 4.5$ μm these are the only screening conditions uniformly used for selection of CDP data suitable for the comparisons.

We define cloud-top height in an ascending (descending) flight segment as the altitude of the point where the aircraft exits (enters) the cloud, i.e., that of the highest point with the CDP data satisfying the above-listed screening conditions. Then, a CDP data segment is selected from the immediate vicinity of the exit (entry) point with the measurement altitudes ranging within 50 m below the cloud top. To select an appropriate data interval for a flight pattern when the aircraft grazes the cloud top without exiting or entering the cloud, we rely on HSRL profiles. After the CDP data interval is selected, we take the RSP data record from the same ground/cloud track and for each RSP data point locate the nearest point in the CDP interval within the RSP measurement spacing (if such a point does exist). The results of comparisons (means and standard deviations of r_{eff} and v_{eff}) between the RSP and CDP datasets selected using the above-described procedure are presented in the next section and in Table 1. In addition to comparisons of CDP data with RSP retrievals made using the parametric algorithm, we also compare them with parameters of one of the modes of RFT-derived DSDs. The latter comparisons may have advantages in the cases of two-layer cloud systems, when DSDs sampled by CDP in one layer correspond to only one mode of the bimodal DSDs retrieved from RSP data. Parametric RSP retrievals in such cases show values of v_{eff} (large) and r_{eff} which are not representative of either of the size modes.

In addition to comparison of DSD statistics (r_{eff} and v_{eff}), we will show examples of remotely sensed and *in situ* DSDs themselves. The metric Δ (Alexandrov et al., 2010, 2012b) will be used for quantitative comparison of the shapes of the normalized droplet size distributions $n_{RSP}(r)$ and $n_{CDP}(r)$:

$$\Delta = \frac{1}{2}\int_{0}^{\infty} |n_{RSP}(r) - n_{CDP}(r)| \; \mathrm{d}r. \tag{4}$$

The value of Δ varies between zero (for identical DSDs) and one (for distributions without common support). This metric responds to both systematic and random discrepancies between two distributions. Given the uncertainties in both RSP and *in situ* data we consider comparisons for which $\Delta \lesssim 20\%$ as showing good agreement between the two size distributions and comparisons with $\Delta \lesssim 30\%$ as showing acceptable agreement. Note that the single-point plots comparing DSD shapes serve only as illustrations and subjects for discussion, while quantitative results presented in Table 1 are based on entire sets of all *in situ* samples made within 50 m from cloud top.

While the RSP and CDP sampling volumes are different, the horizontal linear sizes of their samples are similar (70 vs. 110 m), so the effects of horizontal inhomogeneity on comparisons are not expected to be significant. The sharp vertical profiles of droplet size parameters appears to present the greatest challenge for comparisons, requiring careful selection of *in situ* data from cloud tops. Other uncertainties can be caused by differences in measurement times and locations. Remote sensing and *in situ* measurements were made on co-located ground tracks, while at different times (up to 1 h apart). This can raise questions as to whether the cloud field shifted from its initial location or otherwise changed during the time between the measurements. Fortunately, on three out of four days reported in this study the validation segments were flown over vast stratocumulus cloud decks known for their steadiness and spatial homogeneity. Also, NASA GOES satellite images made with one-hour interval between them show no visible changes in cloud fields in the vicinities and at times of the measurements. We should also note that the good intercomparison results obtained in this study can be themselves considered as an evidence of successful co-location of RSP and CDP data.

4. Case studies

Several good opportunities for direct inter-comparisons between remote sensing retrievals and cloud-top *in situ* measurements of cloud DSDs occurred during the second NAAMES deployment: on May 18, 20, 27, and 30 of 2016. These cases are described below and summarized in Table 1. Plots of the RSP and CDP datasets being compared in each case are presented in Supplemental material accompanying this paper.

4.1. May 18, 2016

The first opportunity for intercomparison of RSP and *in situ* retrievals of cloud droplet size distributions was on May 18. The C-130 flew two

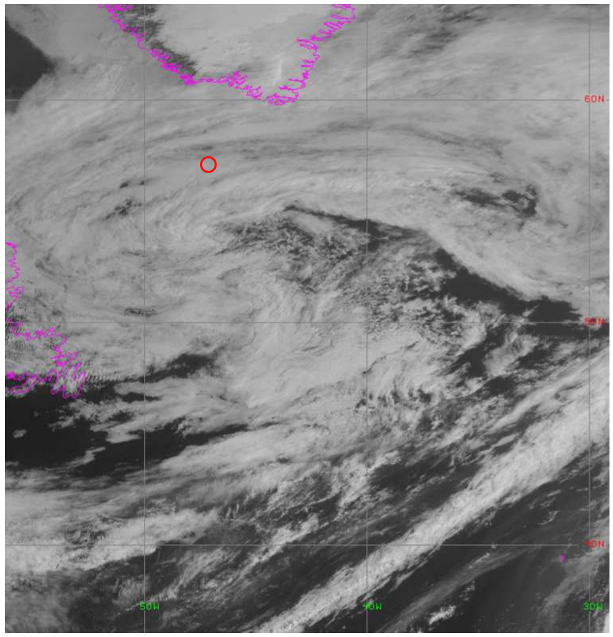

Figure 2: GOES satellite image of North Atlantic ocean for 11:15 UTC on May 18, 2016. The coastline of Newfoundland is shown in the West, while that of Greenland – in the North. The vicinity of the validation flight segments is depicted by red circle.

co-located legs between the points with coordinates (56.7°N, 45.2°W) and (57.0°N 47.2°W). The high-altitude leg during which RSP and HSRL measurements were made was flown between 10:58:17 and 11:11:56 UTC, while the low-altitude leg that provides characterization of the marine boundary layer and clouds by CDP and other *in situ* measurements was flown about one hour later, between 11:48:00 and 12:04:12 UTC. Figure 2 presents GOES satellite image of the cloud systems in the vicinity of the described flight legs. The site of interest is located within a large low-pressure system spreading between Newfoundland and Greenland. The center of this system at the time of the measurements was just south of the site, with the occluded front wrapped around to the north. The region of interest is dominated by stra-

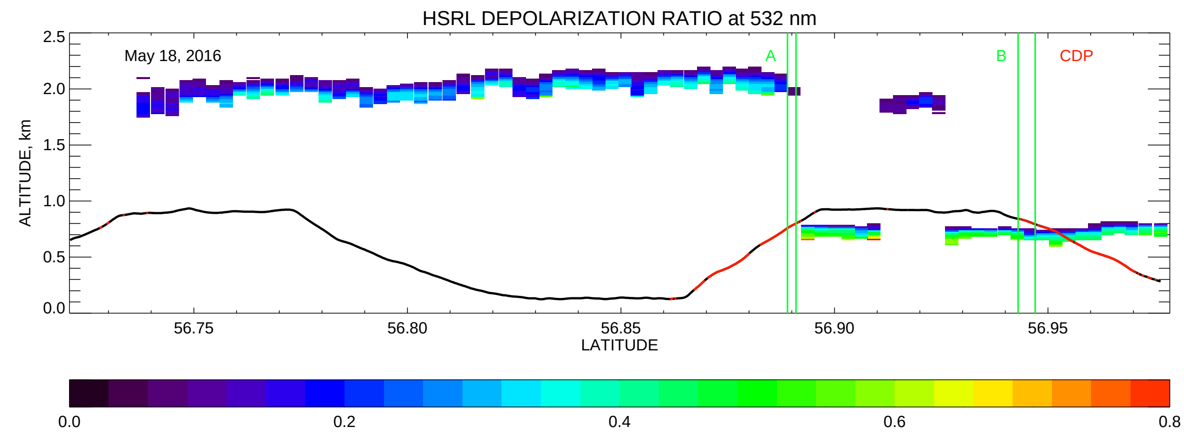

Figure 3: HSRL depolarization ratio profile for the May 18 case. Black curve depicts the altitude of the aircraft during the *in situ* segment. Red points on this curve indicate availability of CDP measurements with $r_{\text{eff}} > 4.5$ μm. The pairs of vertical green lines labeled A and B indicate the intervals used for RSP-CDP intercomparisons presented in Table 1. The DSDs from the top points of these intervals are shown in Fig. 5.

tocumulus (Sc) clouds.

The aircraft altitude during the *in situ* segment is plotted in Fig. 3 (black curve) as function of latitude. The points where CDP measurements are available with $r_{\text{eff}} > 4.5$ μm (indicating in-cloud data) are highlighted in red. Figure 3 also shows volume depolarization ratios (VDRs) for the same geographical locations derived from HSRL measurements at 532-nm wavelength that were made during the remote-sensing leg. They indicate the cloud tops in the observed scene. Two layers of clouds are clearly seen in this plot with cloud tops at approximately 0.8 km and 2 km, respectively. Only the lower-layer cloud was sampled by CDP, while RSP was able to observe both layers when the top one was optically thin.

The results of parametric RSP retrievals of the droplet effective radii and

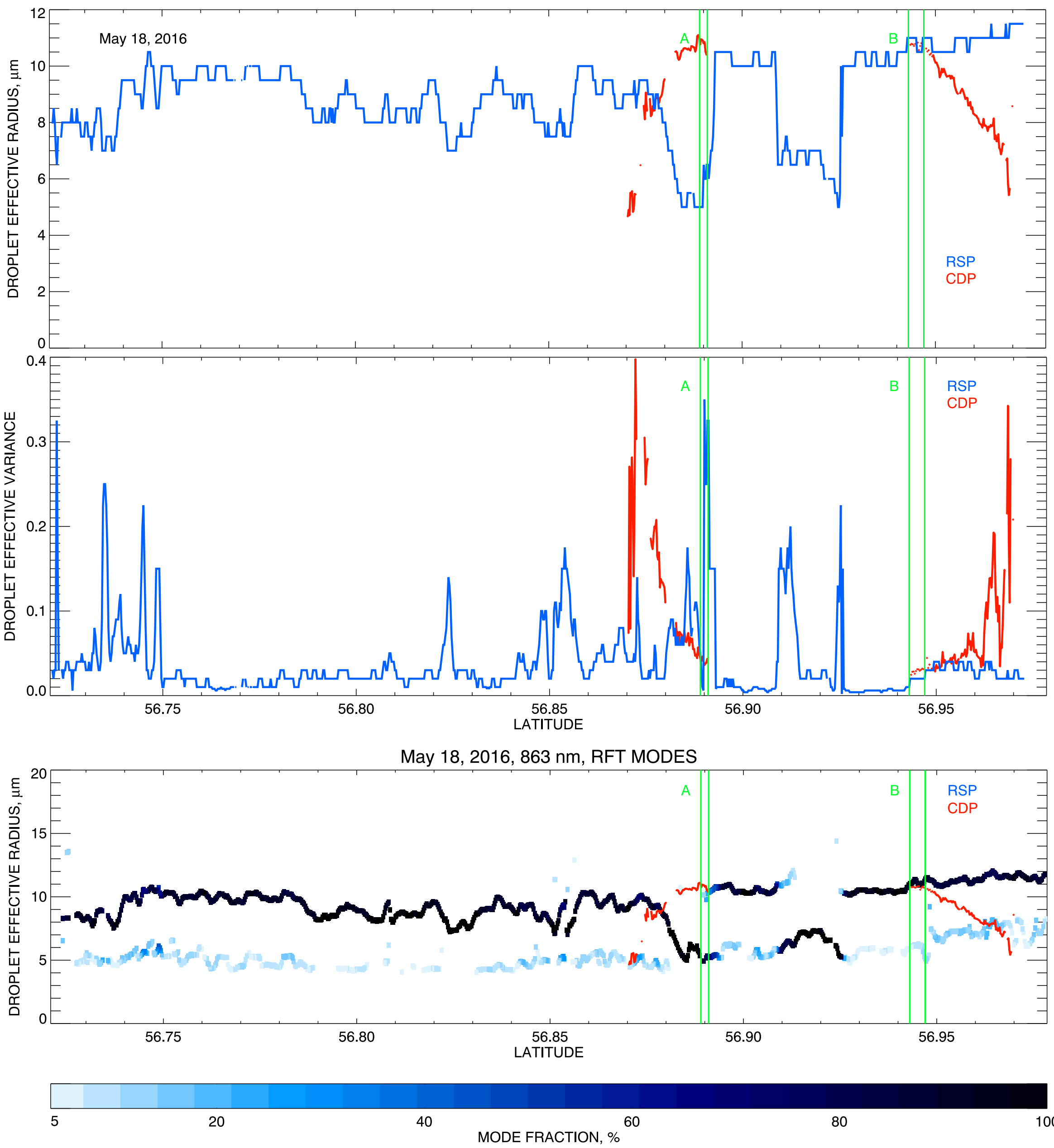

Figure 4: Top and middle: effective radius and variance, respectively, retrieved from the RSP data using the parametric fitting technique (blue curves). The discretization seen in these plots is that of the LUTs used. Bottom: the results of mode decomposition applied to distributions derived from RSP data using RFT. The curves depicting the modes' effective radii are colored according to the modes' respective weights in DSD. The red curves in all panels depict the screened co-located CDP retrievals. The pairs of vertical green lines labeled A and B indicate the intervals used for RSP-CDP intercomparisons presented in Table 1.

variances are presented in Fig. 4 (top and middle), while the RFT retrievals from the RSP data (effective radius and fraction of each mode in total DSD) are shown in the bottom panel. The correlative screened CDP data is plotted in all three panels (red curves). These plots show unmistakable similarity in the positions of sharp changes in droplet size with those of gaps in the upper cloud layer identified in the HSRL profile (Fig. 3). For example, the short isolated segment of the upper layer between latitudes 56.91°N and 56.93°N coincides with the sharp drop in RSP-derived r_{eff} from 10 to 7 μm in parametric retrievals and with strengthening of the 5-6-μm size mode in RFT results (while the 10-μm-mode disappears). This allows us to associate the smaller mode in DSD with the upper layer and the larger one – with the lower layer. Unfortunately, the upper layer had not been sampled by the CDP, so only the RSP retrievals for the lower layer can be validated.

Figures 3 and 4 suggest that our choice for quantitative intercomparison of RSP and CDP retrievals near cloud top in this case is limited to two locations (indicated in the plots by two pairs of vertical green lines): (A) the exit from the cloud (11:59 UTC, Lat: 56.89°N) and (B) the entrance back into cloud at (12:02 UTC, Lat: 56.94-56.95°N). The results of the RSP-CDP comparisons for the intervals when CDP was less than 50 m below cloud top are presented in Table 1, while the examples of the RSP- and CDP-derived DSDs for the highest points of locations A and B are shown in Fig. 5 (top and bottom panels, respectively). The left panels of Fig. 5 show the droplet number distribution (from parametric fit for RSP) and right panels - the droplet area distributions (from RFT for RSP).

Figure 5 (top right) indicates that the RSP-derived DSD in case A is

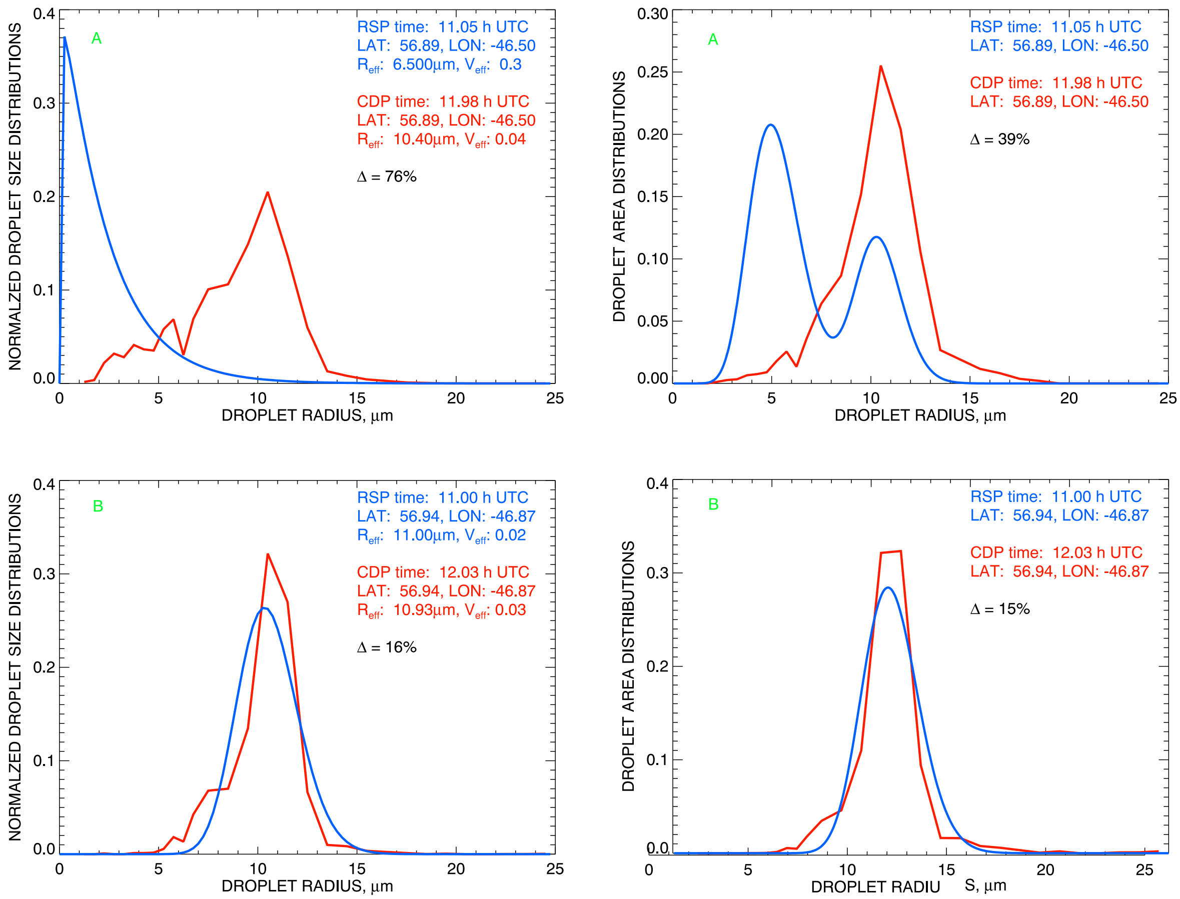

Figure 5: RSP- (blue) and CDP-derived (red) droplet number (left) and area (right) distributions corresponding to cloud exit (A: 11.98 h UTC, top) and entrance (B: 12:03 h UTC, bottom) in the May 18 case (see Fig. 3). The presented RSP retrievals are parametric in left plots and RFT-derived in right plots.

essentially bimodal with dominant 5-μm mode attributed to the upper cloud layer (which was not sampled *in situ*). In parametric retrievals (Fig. 5 (top left)) this corresponds to small $r_{\rm eff} = 6.5$ μm and very large $v_{\rm eff} = 0.3$ (which also skews the gamma distribution shape to the left) (cf. Alexandrov et al., 2015, 2016a). The reason for this bimodality is in the overlap between the upper and lower cloud layers seen in the HSRL profile (Fig. 3), which results in both layers simultaneously contributing to the RSP measurements. Table 1 indicates that this problem affects parametric RSP retrievals in the whole 9-point interval at cloud top yielding r_{eff} of 5.56 μm on average (vs. 10.80 μm for CDP) and v_{eff} of 0.10 (vs. 0.04 for CDP). This means that validation of parametric RSP retrievals fails in this case, however, the parameters of the larger size mode in the RFT-derived DSD can still be compared with *in situ* measurements since they both correspond to the same lower layer of clouds. Figure 5 (top right) indicates that the larger RFT mode has a similar shape to the whole CDP-derived distribution (they differ only by a constant normalization factor). Quantitative comparison for the the whole interval in Table 1 also shows much better results (presented in parentheses): RSP's average r_{eff} of 10.75 μm and v_{eff} of 0.01, which corresponds to average RSP-CDP bias in r_{eff} of -0.02 μm (0.85 μm standard deviation); and in v_{eff} of -0.02 (0.006 standard deviation).

In case B the lower cloud layer was scarcely obscured by the top one, so CDP and RSP observed droplets in the same cloud layer. This resulted in good agreement between RSP (both parametric and RFT) and CDP retrievals for the 15-point interval at cloud top. Table 1 shows the RSP's parametric r_{eff} of 10.80 μm on average vs. 10.77 μm for CDP (0.035 μm mean difference, 0.26 μm standard deviation); and RSP v_{eff} of 0.02 on average vs. 0.03 for CDP (-0.01 mean difference, 0.002 standard deviation). Fig. 5 (bottom) shows that the DSD shapes for the two instruments also agree well ($\Delta = 16\%$) at the highest point of the interval B. Note that in this particular DSD example the RFT yielded no smaller size mode, while

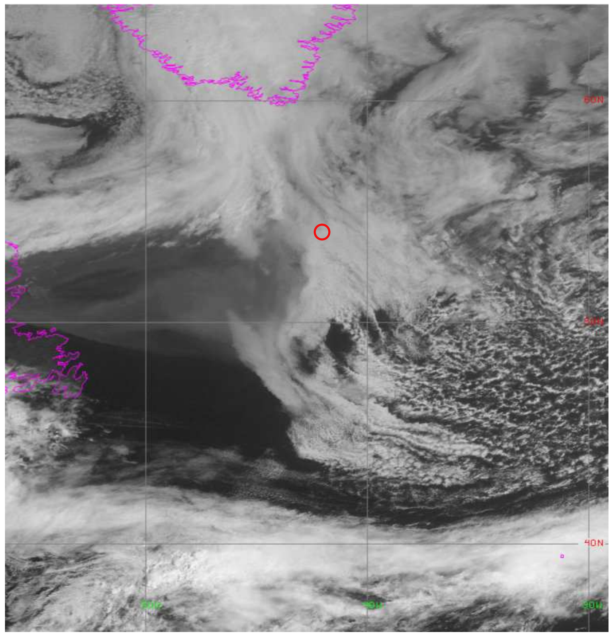

Figure 6: Same as Fig. 2 but for 12:45 UTC on May 20, 2016.

for the rest of the interval it constituted 8–12% of the DSDs, as can be seen in Fig. 4 (bottom).

4.2. May 20, 2016

The validation segments flown on May 20 have similar structures to those from May 18 with the aircraft porpoising though the full depth of the cloud. The flight legs were located between points with coordinates (53.2°N, 41.1°W) and (54.3°N, 42.3°W). The high- and low-altitude legs were flown during the 12:43:55–12:52:58 UTC and 13:17:24–13:37:12 UTC time intervals respectively. The GOES satellite image in Fig. 6 shows cloud fields at and around the measurement site. The site is located in between frontal systems, with a region of high pressure to the south-southeast and a series of

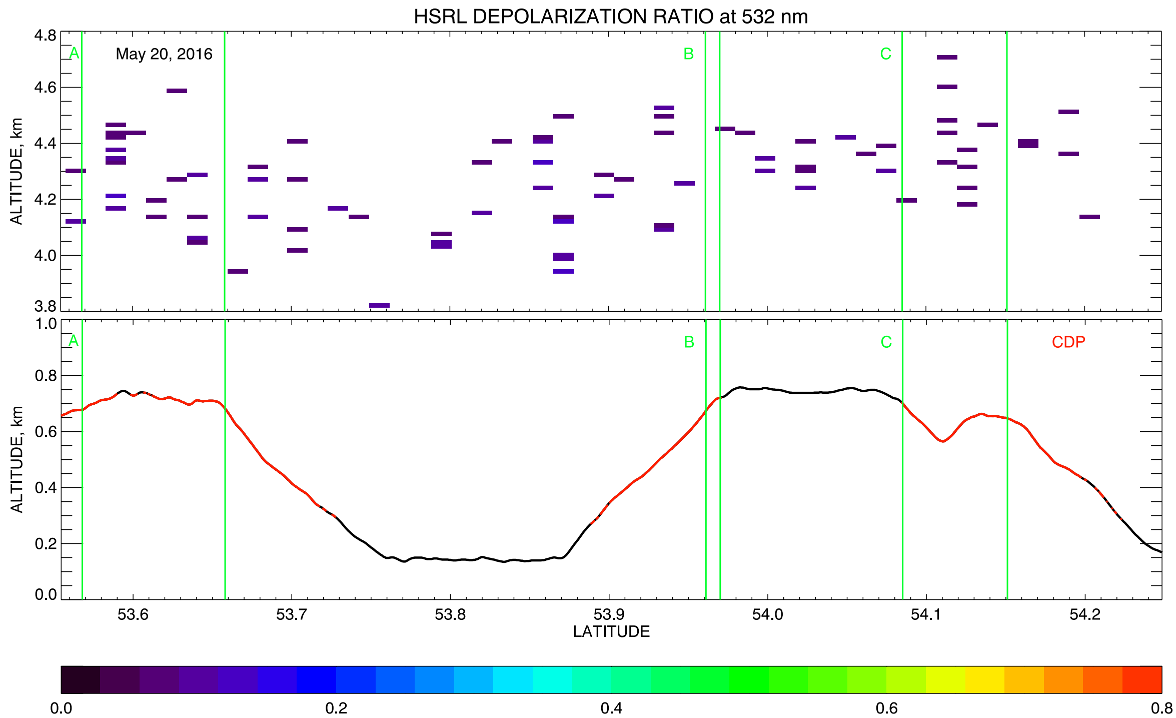

Figure 7: Same as in Fig. 3 but for May 20, 2016 case. The pairs of vertical green lines labeled A, B, and C indicate the intervals used for RSP-CDP intercomparisons presented in Table 1. The DSDs from the top points of these intervals are shown in Fig. 9.

weak low-pressure systems to the east. The site is dominated by Sc clouds which are either induced by these low-pressure systems, or are moving into the region ahead of a cold front over the Labrador Sea.

Figure 7, similar to Fig. 3, shows the altitude of the lower leg and the availability of *in situ* cloud data (red points). While the presence of cloud data clearly indicates that the aircraft was porpoising though clouds with tops of about 750 m and bottoms of 300 m, these clouds are not visible in HSRL profiles in Fig. 7. However, the low cloud layer can be clearly seen

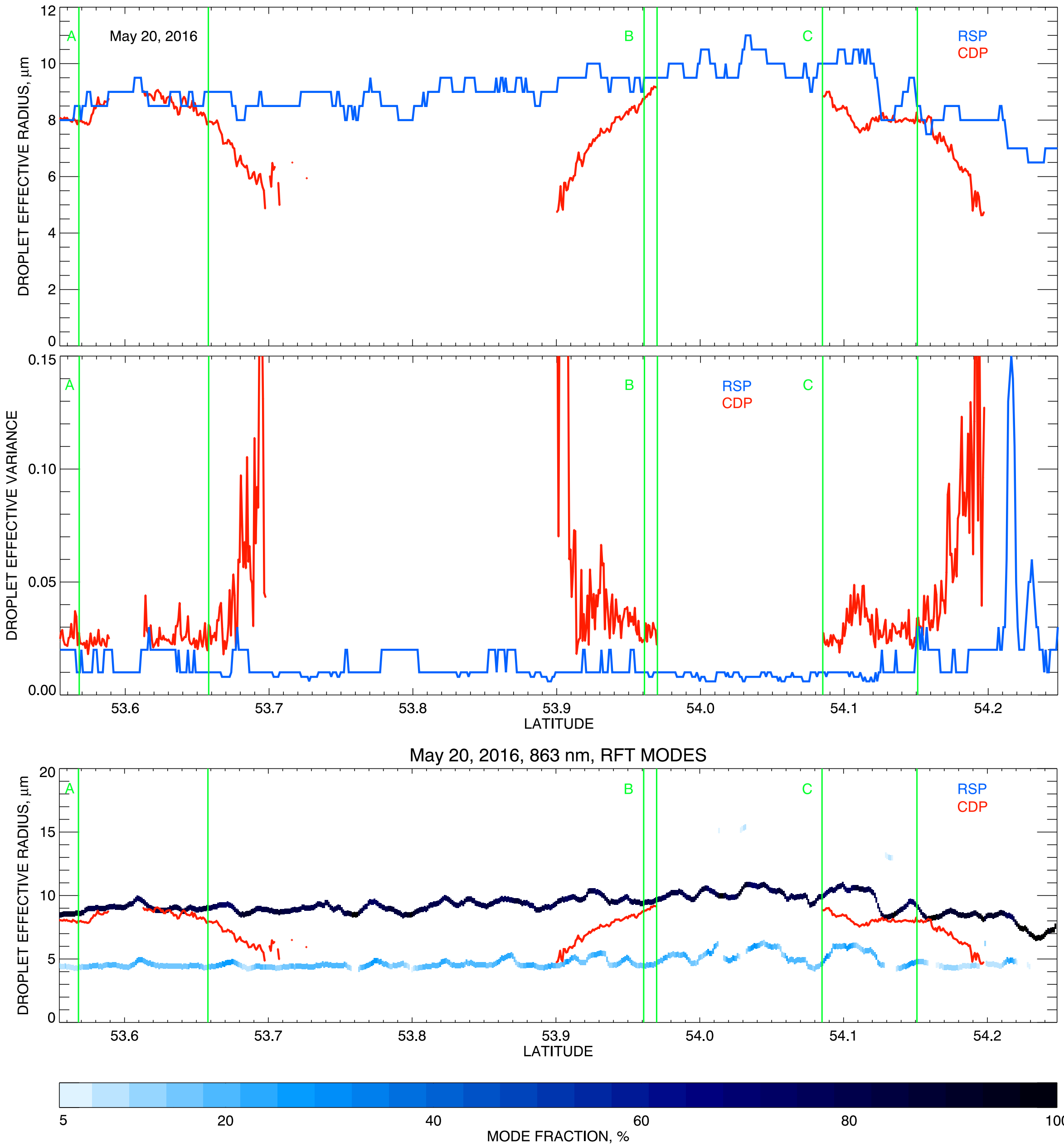

Figure 8: Same as in Fig. 4 but for May 20, 2016 case. The pairs of vertical green lines labeled A, B, and C indicate the intervals used for RSP-CDP intercomparisons presented in Table 1.

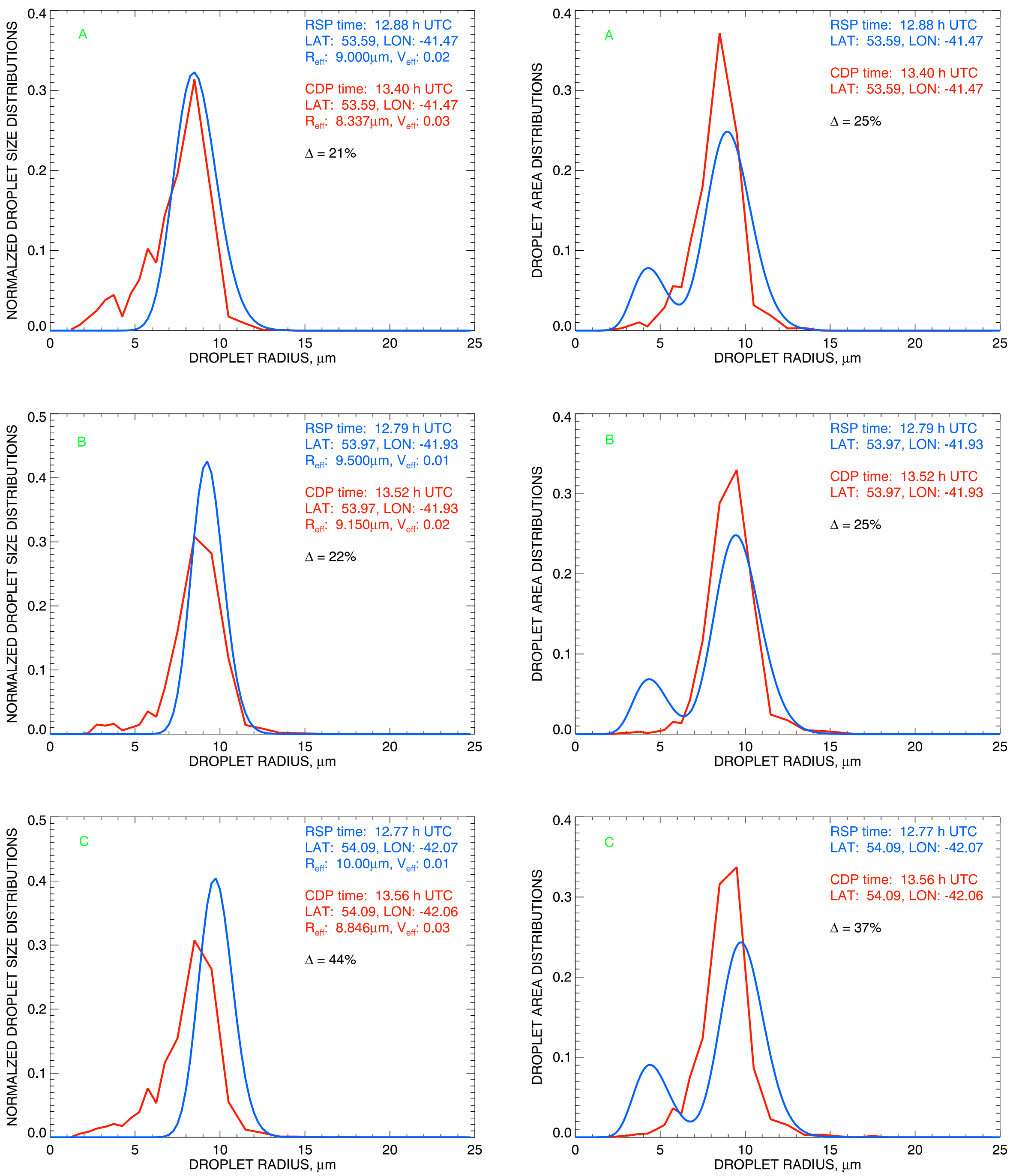

Figure 9: RSP- (blue) and CDP-derived (red) droplet radius (left) and area (right) distributions corresponding to cloud top (A: 13.40 h UTC, top); exit (B: 13.52 h UTC, middle); and entrance (C: 13.56 h UTC, bottom) in the May 20 case (see Fig. 7). The presented RSP retrievals are parametric in left plots and RFT-derived in right plots.

if HSRL's low-signal mask is not applied (see Supplemental material) despite the presence of noise in the picture. The most likely reason for such weak signature of the low clouds in HSRL profile is attenuation of the lidar signal by a cloud layer at 4.5 km height, which is apparent in the HSRL 532 nm VDR shown in Fig. 7 (top). The low (less than 0.04) VDR values normally correspond to liquid cloud phase. While on this particular flight HSRL measurements may be affected by accidental contamination of the window with oil from the aircraft, the air temperature of about $-20°$C at 4.5 km is consistent with supercooled liquid water or mixed-phase cloud (cf. Alexandrov et al., 2016a). Thus, the upper layer is expected to contribute a secondary size mode to the RSP-derived DSD making it bimodal. Alexandrov et al. (2016a) reported a similar case when a mixed-phase cloud was observed above a water cloud. In that case a 5-μm mode in bimodal DSD was attributed to the upper layer, while a larger 10-μm mode – to the lower layer.

As in the May 18 case, the RSP retrievals of DSD parameters are in good agreement with CDP measurements when the *in situ* measurements are being made within 50 m from cloud top. Figure 8, where the results of the parametric fit and RFT methods applied to RSP data are compared with CDP retrievals, indicates three such intervals within the segment (depicted by labeled pairs of vertical green lines in Figs. 7 and 8): (A) C-130 ascending to the cloud top and remaining there for a while before descending back into cloud (13:23-25 UTC, Lat: 53.57-53.66°N); (B) exit from the cloud (13:31 UTC, Lat: 53.96-53.97°N); and (C) entrance into the cloud (13:33-35 UTC, Lat: 54.09-54.15°N; note that the part of the interval where CDP was below

50 m was not used in comparisons, see Supplemental file for details). The results of the comparisons between the RSP and CDP retrievals of the droplet effective radius and variance for these three intervals are presented in Table 1 (the values corresponding to the larger size mode in RFT-derived DSDs are placed in parentheses). In all three cases RSP retrievals show slightly larger droplet sizes than *in situ* measurements with the largest bias in effective radius of 0.77 μm (1.00 μm for RFT) in case C. The RSP-derived values of v_{eff} are biased lower by 0.01-0.02 on average compared to those from CDP.

Figure 9 presents examples of DSD shapes derived for the top points of the three intervals. The RFT analysis results shown in the right panels of Fig. 9, as well as Fig. 8 (bottom), strongly indicate the presence of a second smaller (4.5-μm) mode in the cloud DSDs, while the larger (9–9.5-μm) mode is consistent with *in situ* data (cf. Alexandrov et al., 2016a). This smaller mode may be attributed to the 4.5-km cloud layer seen in Fig. 7 (top), implying that this layer is optically thin. Unfortunately, the size of this mode cannot be validated *in situ*, since the upper cloud layer was not sampled. We should note that the parametric algorithm has a tendency to ignore the second mode when it is weak, thus, retrieving the parameters of the dominant mode alone (see Alexandrov et al. (2012a) for more details and simulation results). This is why the parametric RSP results for May 20 agree with those from RFT analysis (both presented in Table 1) on average within 0.3 μm in r_{eff} and within 0.01 in v_{eff}.

4.3. May 27, 2016

The measurements made during the legs flown on May 27 at 15:06:05–15:12:20 UTC (RSP) and 14:39:00–14:46:48 UTC (CDP) resulted in the most

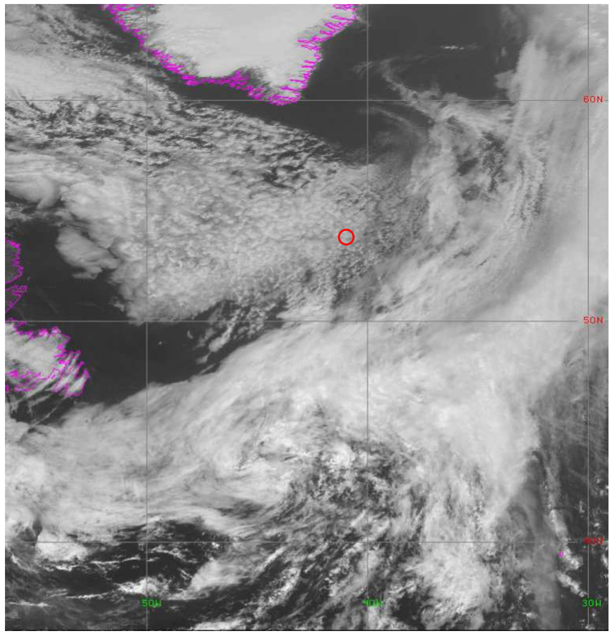

Figure 10: Same as Fig. 2 but for 15:15 UTC on May 27, 2016.

extensive (166 RSP scans) dataset from NAAMES campaign suitable for comparison between remote sensing and *in situ* retrievals, as the aircraft was grazing cloud tops during the *in situ* leg. The RSP and CDP ground tracks were between the points with coordinates (53.7°N, 41.3°W) and (54.3°N, 41.3°W). The GOES image of the observed cloud field and its vicinity is presented in Fig. 10. The measurement site is located in a region just behind a cold front that passed through the region. The general wind flow is coming down the Labrador Sea, bringing closed-cell Sc clouds behind the front. The distance between the tracks of high-altitude and low-altitude legs in this case was larger than in the other three cases (up to 1 km vs. 200 m). However, the homogeneity of the Sc cloud field means that discrepancies between *in situ* and remotely sensed DSDs caused by spatial mismatches in

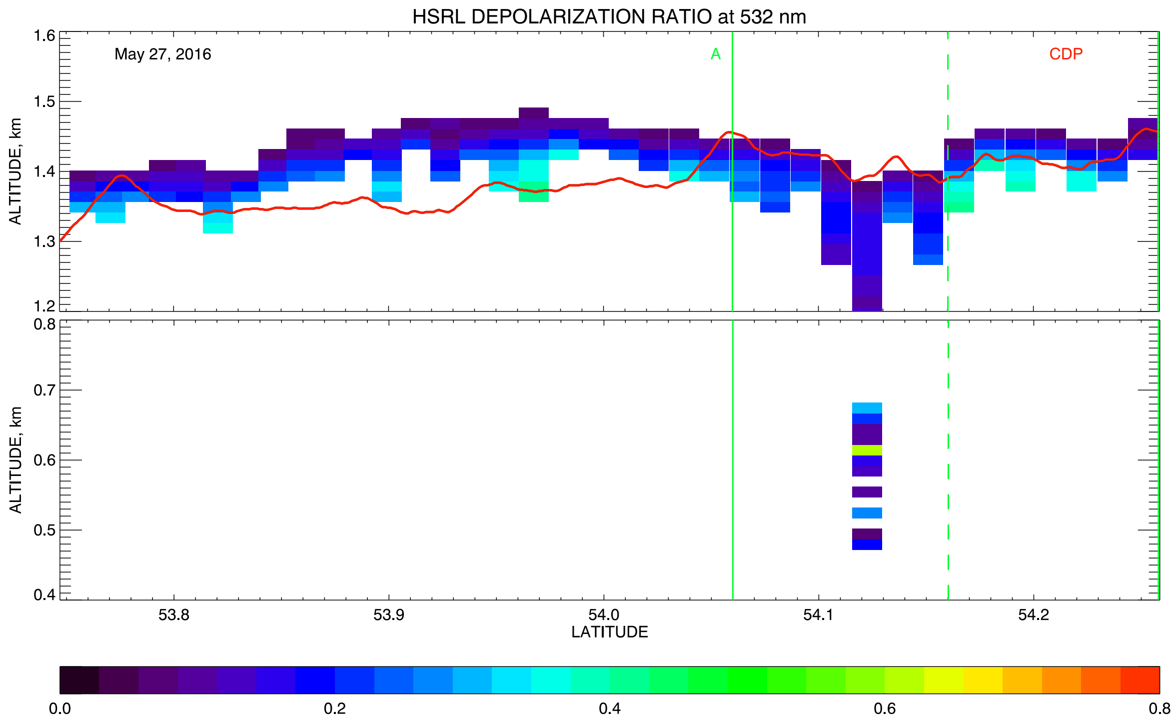

Figure 11: Same as in Fig. 3 but for May 27, 2016 case. Two solid vertical green lines bound the single interval (A) used for comparisons. This two lines together with dashed line between them represent points used in DSD shape comparisons shown in Fig. 13.

the horizontal are expected to be minimal.

For quantitative comparisons of DSDs effective radius and variance (Fig. 12) we selected the parts of the legs north of 54.06°N where the aircraft was close to cloud top during the *in situ* leg, as is seen in Fig. 11. Note that unlike other cases considered in this study, the C-130 had not exited or entered the cloud during the *in situ* segment, so we cannot determine the exact cloud top based on CDP data themselves. Thus, in this case our selection of the CDP data to compare with the RSP retrievals is based on HSRL profiles.

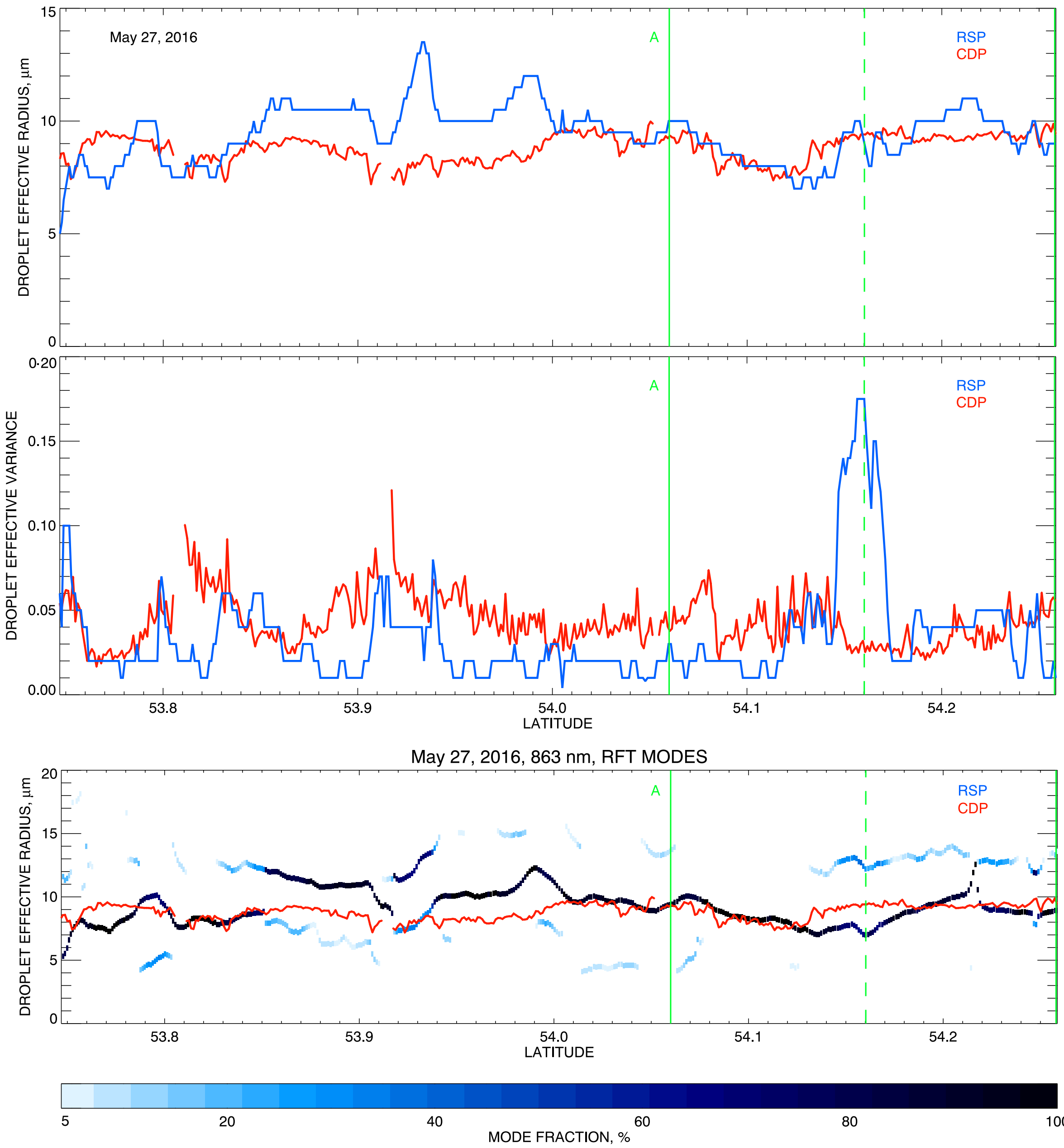

Figure 12: Same as in Fig. 4 but for May 27, 2016 case. Two solid green lines bounding the comparison interval and dashed line between them represent points used in DSD shape comparisons shown in Fig. 13.

In the absence of clearly identifiable data points (such as cloud entry or exit) we rather arbitrarily chose the examples for comparison of DSD shapes (Fig. 13) from the first (top panels) and the last (bottom panels) points of the selected interval. In addition to this, Fig. 13 (middle) presents the DSDs from the point in the middle of the interval depicted by a dashed vertical green line in Figs. 11 and 12. This point was chosen because of strong bimodality of the RFT-derived distribution shape (which is discussed below).

The results presented in Table 1 show that in the selected interval the RSP's r_{eff} is practically unbiased relative to the CDP retrievals, while the standard deviation of the difference between RSP and CDP values was relatively large compared to other cases (0.82 μm for parametric, 1.00 μm for dominant RFT mode). The difference in effective variance between *in situ* and remote sensing retrievals is very small on average (less than 0.01), however the standard deviation of the differences is quite large (0.04) when parametric RSP retrievals are used. This is mostly due to the peak in RSP's v_{eff} around 54.16°N in latitude (Fig. 12 (middle)) reaching values as high as 0.18. As in the May 18 case A, such high variances are associated with a distinctively bimodal structure of the RFT-derived DSDs (Figs. 12 (bottom), 13 (middle)), when the parametric fit reflects the width of the whole size distribution rather than the dominant mode (which has smaller v_{eff} close to the CDP value).

We usually associate bimodal DSDs with two-layer cloud systems, and in this case there is a feature in HSRL data that can be interpreted as signature of a second cloud layer. Figure 11 (bottom) shows a single lidar profile of a

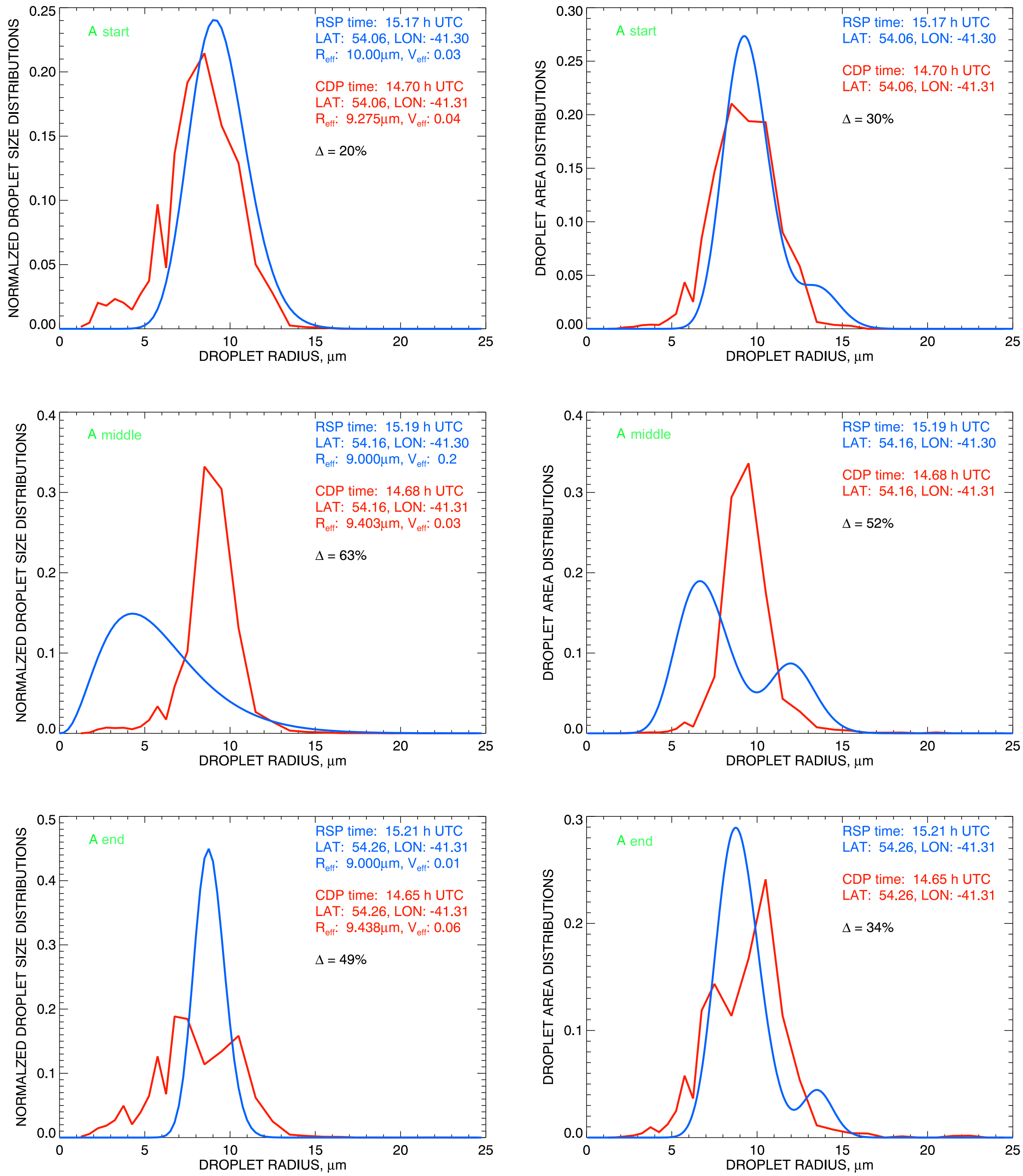

Figure 13: RSP- (blue) and CDP-derived (red) droplet radius (left) and area (right) distributions selected from May 27 data. The CDP time stamps for these examples are 14.70 h UTC (top), 14.68 h UTC (middle), and 14.65 h UTC (bottom). The presented RSP retrievals are parametric in left plots and RFT-derived in right plots. The top and bottom plots correspond to the ends of the comparison interval (solid green lines in Figs. 11 and 12), while the middle plots show distinctly bimodal DSD from the middle of the interval (depicted by dashed line in Figs. 11 and 12).

layer with top at about 700 m located below the cloud which was sampled (this signature is wider when HSRL's low-signal mask is off: see Supplemental material). Note that the reported profile of the top layer (Fig. 11 (top)) at this point goes deeper into the cloud (to 200 m below cloud top) than in the rest of the segment. This indicates that the cloud top is optically more diffuse here allowing the laser signal reflected from deeper into the cloud and possibly the bottom layer to be detected. The DSD modes can be attributed to the two layers based on Fig. 12 (bottom)). There the dominant 9-μm size mode continuously extends to the part of the interval where it becomes the sole mode detected by the RSP. This happens only where the bottom layer is not detectable by the instrument (see also Fig. 13 (top)). Thus, we attribute the smaller droplet size mode to the top cloud layer and the larger 12-μm mode to the bottom layer. This attribution is also consistent with Fig. 12 (bottom) where the *in situ* droplet sizes sampled in the top layer are much closer to these of smaller mode in RFT-derived DSD than to those of the larger mode. The top heights of the two cloud layers and the droplet sizes in them are similar to those in May 18 case.

4.4. May 30, 2016

The validation segments flown on May 30, 2016 between points with coordinates (43.6°N, 44.7°W) and (44.8°N, 44.0°W) were 25 minutes apart: 14:32:07–14:46:28 UTC (high altitude remote sensing) and 15:09:00–15:32:24 UTC (low altitude *in situ* sampling). The cloud system surrounding the measurement site on this day (Fig. 14) is quite different from the uniform stratocumulus fields observed on the other three days. The site is located in the north-east quadrant of a strong low-pressure system, with a high-

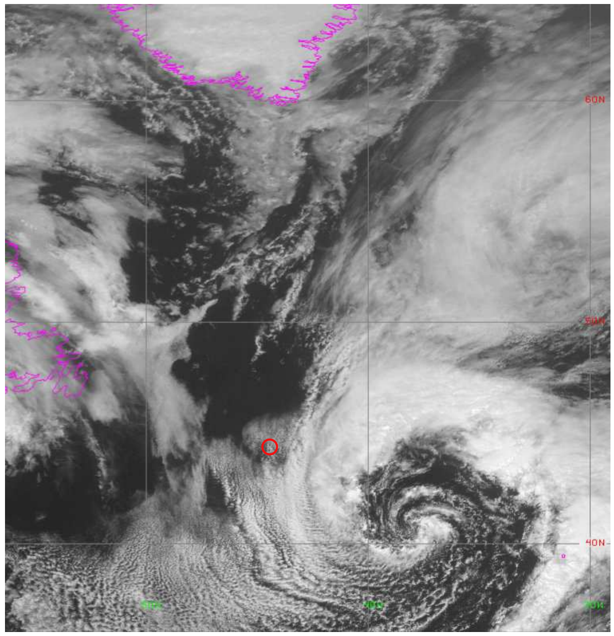

Figure 14: Same as Fig. 2 but for 14:45 UTC on May 30, 2016.

pressure system moving in from the west. On the back end of the system, the northerly flow is mixing in dry air bringing both open-cell and closed-cell Sc clouds.

During the *in situ* leg the aircraft followed the porpoising pattern (Fig. 15) similar to that of May 18 and 20. As in May 20 case, here the CDP droplet size measurements made within 50 m from cloud top are present in three short intervals (indicated by pairs of vertical green lines labeled A, B, and C in Figs. 15 and 16): (A) exiting the cloud (15:18-19 UTC, Lat: 44.09-44.11°N); (B) entering it from above (15:22 UTC, Lat: 44.21-44.22°N); and (C) crossing a thin part of the cloud (15:29 UTC, Lat: 44.65-44.66°N).

The complexity of cloud morphology in the May 30 case seen in Fig. 14 also shows up in the HSRL profiles (Fig. 15) as highly heterogeneous cloud

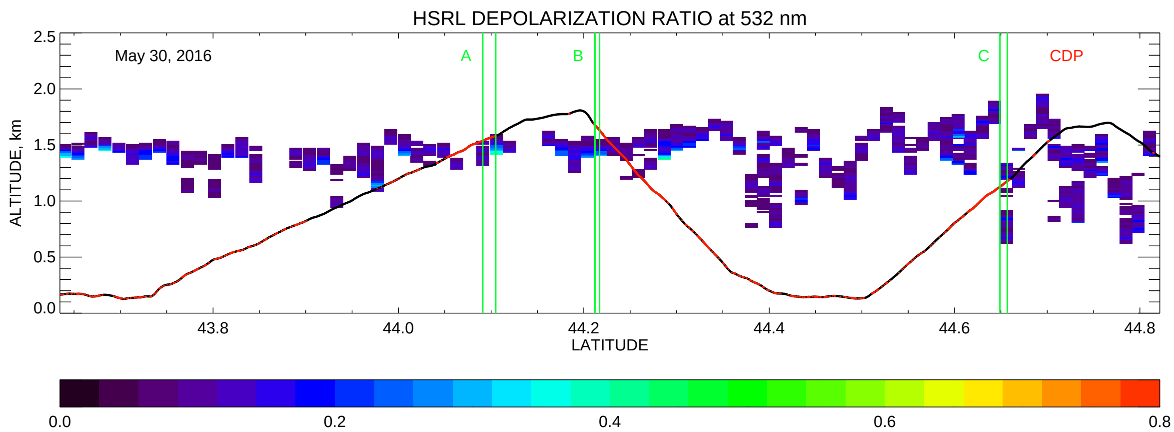

Figure 15: Same as in Fig. 3 but for May 30, 2016 case. The pairs of vertical green lines labeled A, B, and C indicate the intervals used for RSP-CDP intercomparisons presented in Table 1. The DSDs from the top points of these intervals are shown in Fig. 17.

top (especially in the second half of the segment), and in both RSP and CDP droplet size retrievals. Unlike mature marine stratocumulus clouds with very narrow DSDs at cloud top seen on May 18, 20, and 27, here we encounter very diverse cloud microphysical structure characterized by wide DSDs for which the parameters rapidly change from point to point (Figs. 16 and 17). Using such a dataset for an RSP-CDP intercomparison presents certain challenges because the spatial and temporal heterogeneity of cloud DSDs may lead to large discrepancies between the two types of retrievals due to greater than 15 minute difference in observing times and/or $\sim$ 200 m spatial mismatches between the observation locations. Thus, this case tests the limits of cloud system complexity under which we can still expect good agreement between remote sensing and *in situ* retrievals.

Despite the above concerns, the RSP-CDP agreement in the three specified cloud-top cases appears to be reasonably good (Table 1). In cases A

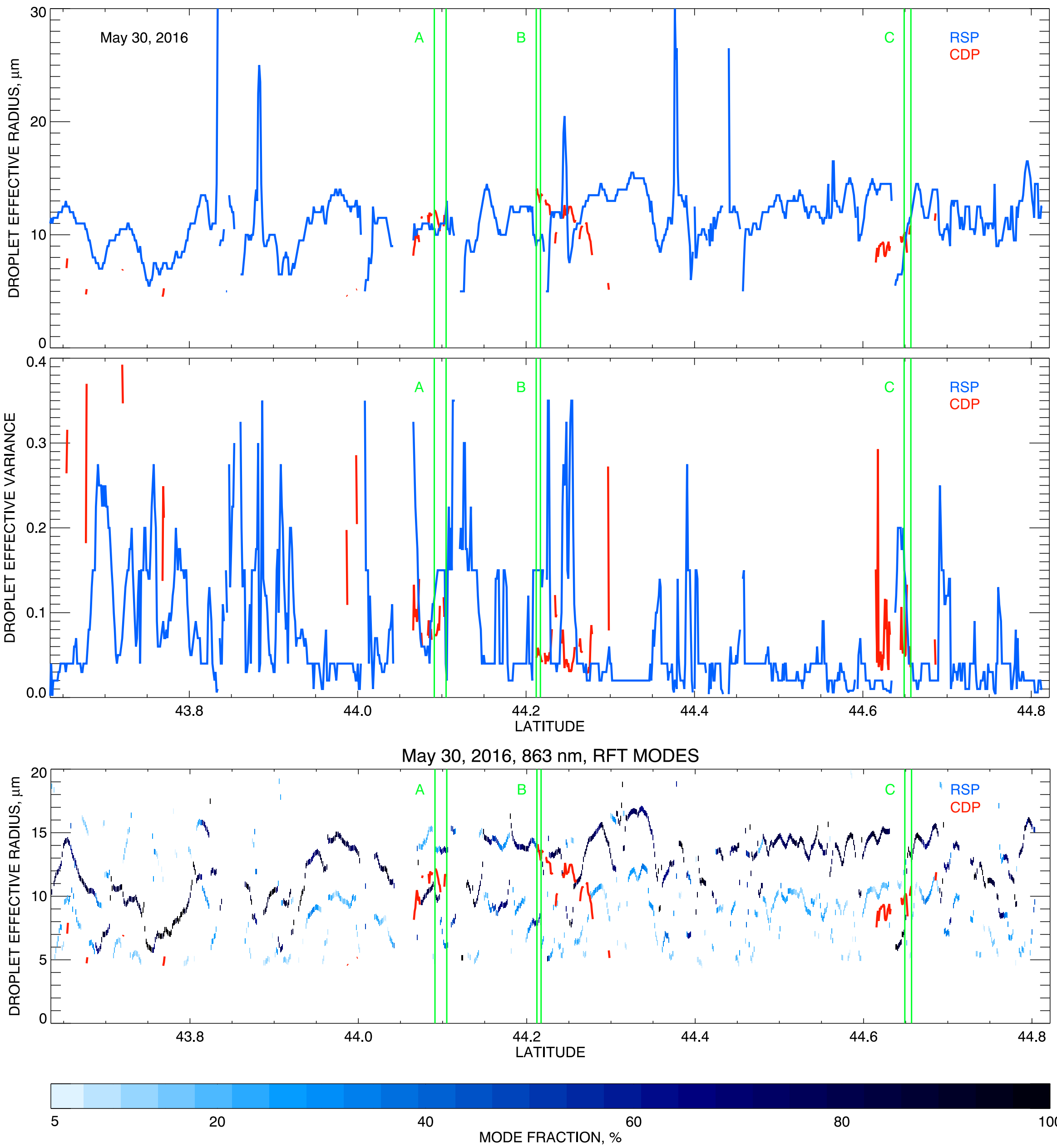

Figure 16: Same as in Fig. 4 but for May 30, 2016 case. The pairs of vertical green lines labeled A, B, and C indicate the intervals used for RSP-CDP intercomparisons presented in Table 1.

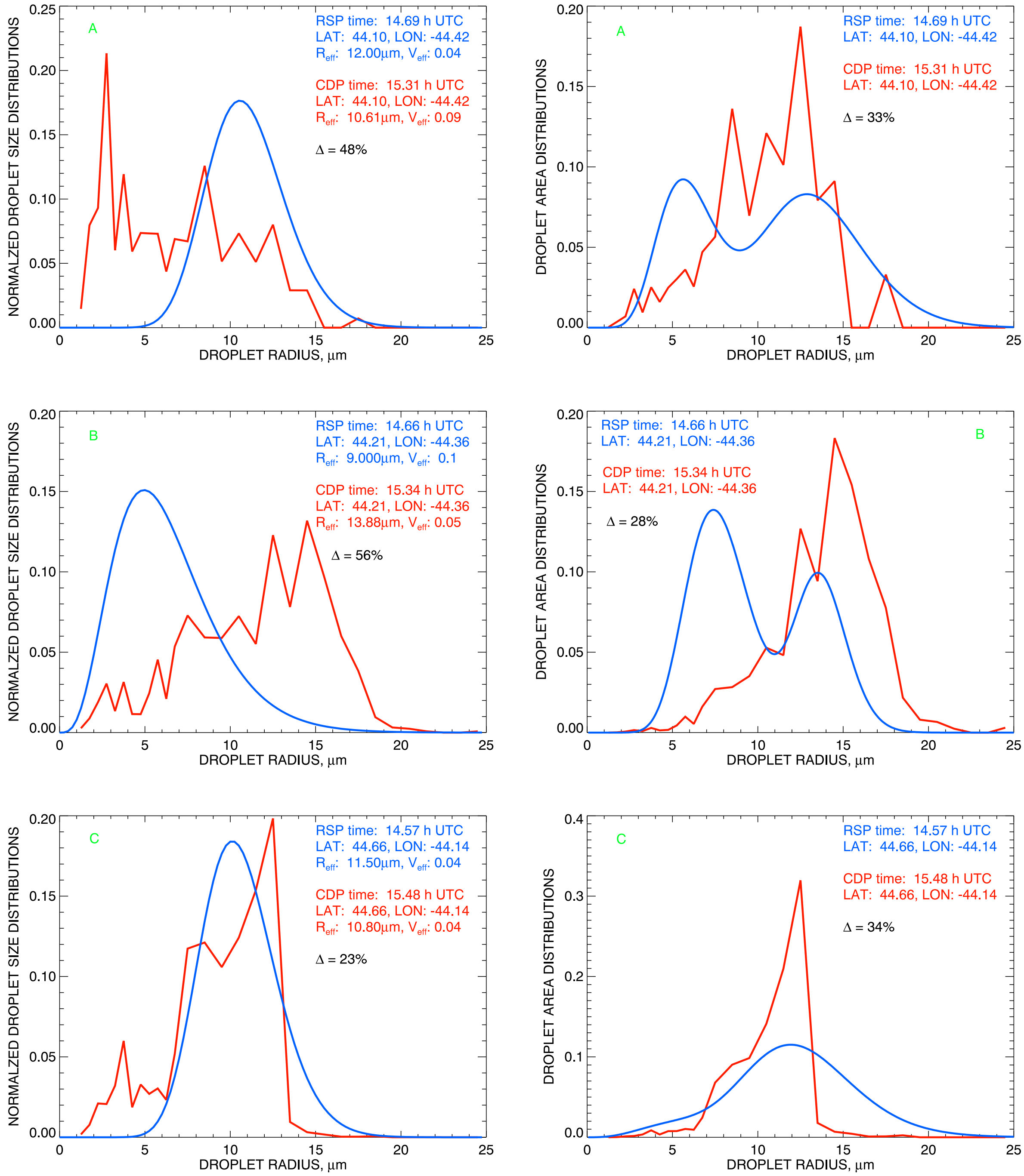

Figure 17: RSP- (blue) and CDP-derived (red) droplet radius (left) and area (right) distributions corresponding to the aircraft exiting the cloud top (A: 15.31 h UTC, top); entering the cloud from above (B: 15.34 h UTC, middle); and crossing a thin part of the cloud (C: 15.48 h UTC, bottom) in the May 30 case (see Fig. 15). The presented RSP retrievals are parametric in left plots and RFT-derived in right plots.

and C the RSP (parametric) and CDP results show relative biases in effective radii of ~ 0.5 μm with the standard deviations of the differences being $\sim$1 μm. The RSP-derived $v_{\rm eff}$ appear to be larger on average than those in CDP retrievals by 0.02–0.04 with standard deviations of the differences up to 0.05, however, we should note that the effective variances themselves were large ($\sim$ 0.1 on average) in both datasets. The magnitude of these differences between RSP-derived and *in situ* DSD parameters, while being larger than on other days, is still acceptable. The DSDs from the top points of the intervals are shown in Fig. 17. We see from Fig. 17 (top right) that RFT analysis in case A yields a distinctively bimodal distribution, while the CDP-derived DSD shows no similarity to either one of the two modes, being rather in between them. Similar situation is encountered in case C, while small mode there is rather weak (and is not seen at all in the cloud-top DSD from Fig. 17 (bottom right)). In both cases A and C parametric RSP retrievals of $r_{\rm eff}$ are in a better agreement with CDP data than the values from any RFT mode, perhaps because two-layer structure is not well-defined in these cases. (Comparisons of CDP-derived parameters with those of both RFT modes in cases A and C can be found in Supplemental material.)

The RFT retrievals should be used instead of the parametric ones in specific cases of distinctively two-layer cloud systems where the CDP makes samples within one of the layers, while the RSP observes both. Cases A and C do not fall into this category (probably due to the complex structure of the clouds), however, case B seemingly does. DSD retrievals in this case very much resemble those in case A from May 18, despite there being no two-layer cloud structure seen in HSRL profiles from Fig. 15. In this case we again see strongly bimodal DSD from RFT analysis with the CDP distribution being close to its larger mode (Fig. 17 (middle right)), while parametric DSD in Fig. 17 (middle left) has much larger v_{eff} (0.1 vs. 0.05) and smaller r_{eff} (9 μm vs. 14 μm) than its CDP counterpart (compare to Fig. 5 (top)). The same situation is repeated for the whole interval B (see Table 1), where the average large RFT mode's r_{eff} of 13.53 μm is much closer to the CDP value (13.51 μm) than the parametric effective radius (9.40 μm). The same is true for the average values of effective variances: 0.15 for parametric RSP retrievals; 0.02 for RFT mode; and 0.05 for CDP.

5. Conclusions

We presented comparisons between cloud droplet size distributions derived from RSP observations with those obtained from the measurements made by the Cloud Droplet Probe. This is the first time that validation of polarimetric droplet size retrievals has been done by direct comparison with correlative *in situ* data. This validation dataset became available because of the targeted flight planning during the NAAMES field campaign (May 2016) when the NASA C-130 aircraft flew over the same ground track twice: one time at high altitude making remote sensing measurements, and the other time at low altitude facilitating *in situ* sampling. The presented comparisons show very good agreement in the cases when both remote and *in situ* measurements were precisely co-located and the aircraft was at cloud top during the sampling. This condition is very important for successful validation since RSP measurements of polarized reflectance are sensitive to cloud droplet sizes only within a layer of unit optical depth (i.e., about 50 m thick) at cloud top, while droplet sizes decrease and DSD widths increase rapidly with depth into the cloud.

It should be noted that while the lack of vertical resolution is common to all airborne passive remote sensing techniques, the localization of the polarimetric retrievals near cloud top is an advantage compared to other methods that provide a weighted average over a generally unknown DSD profile within cloud. Weighting functions in such an averaging depend on optical transmittance of the cloud layer between the altitude of the droplet and cloud top, which itself depends on the unknown DSD profile. In distinction to this, polarimetric measurements allow for direct retrieval of the actual microphysical DSDs, the same as those measured *in situ* or found in the output of a dynamical cloud model.

Four flight segments satisfying the cloud-top sampling condition were selected for detailed intercomparisons. During three of them (May 18, 20, and 30) the aircraft flew in a "porpoise" pattern during the *in situ* leg diving into cloud several times. In such cases the CDP measurements suitable for comparison with RSP were selected at the points within 50 m below the aircraft's entry or exit point at cloud top. In the fourth case (May 27) the aircraft flew at cloud top for some period of time during the *in situ* leg. This made it possible to collect a continuously sampled large dataset for more extensive statistical comparisons with its RSP counterpart.

Two retrieval methods were applied to RSP observations of the polarized rainbow: parametric fitting and non-parametric Rainbow Fourier Transform (RFT), the latter allowing for analysis of complex (in particular, bimodal) DSD shapes. The average values of the DSDs' effective radii and variances

Table 1: Summary of intercomparisons between polarimetric RSP and *in situ* CDP retrievals of effective radii and variances of cloud droplet size distributions from the measurements made during NAAMES field experiment in May 2016. RSP values from parametric fitting algorithm are shown without parentheses, while those from the closest RFT mode are in parentheses. * Cases with two-layer cloud structure where parametric RSP values should not be used (these values are shown in *italics*).

Case No. of pts. CDP pattern at cld. top	CDP Start pt. coord. End pt. coord. Alt. range	RSP $\langle r_{\text{eff}} \rangle$, μm $\langle v_{\text{eff}} \rangle$ Time, UTC	CDP $\langle r_{\text{eff}} \rangle$, μm $\langle v_{\text{eff}} \rangle$ Time, UTC	$r_{\text{eff}}^{RSP} - r_{\text{eff}}^{CDP}$ mean, μm std. dev., μm	$v_{\text{eff}}^{RSP} - v_{\text{eff}}^{CDP}$ mean std. dev.
May 18, 2016					
A* 9 pts. ascent	56.89°N, 46.48°W 56.89°N, 46.50°W 749 – 796 m	*5.56* (10.75) *0.10* (0.01) 11:03	10.80 0.04 11:59	−*5.2* (−0.02) *0.85* (1.5)	*0.1* (−0.03) *0.1* (0.006)
B 15 pts. descent	56.94°N, 46.87°W 56.95°N, 46.90°W 798 – 838 m	10.80 (11.12) 0.02 (0.02) 11:00	10.77 0.03 12:02	0.035 (0.35) 0.26 (0.16)	−0.009 (−0.01) 0.002 (0.002)
May 20, 2016					
A 64 pts. asc/descent	53.57°N, 41.45°W 53.66°N, 41.55°W 679 - 729 m	8.66 (8.96) 0.02 (0.02) 12:52-53	8.51 0.03 13:23-25	0.15 (0.45) 0.44 (0.32)	−0.01 (−0.005) 0.007 (0.004)
B 9 pts. ascent	53.96°N, 41.92°W 53.97°N, 41.93°W 675 – 720 m	9.50 (9.51) 0.01 (0.02) 12:48	8.99 0.03 13:31	0.51 (0.51) 0.17 (0.13)	−0.02 (−0.01) 0.003 (0.003)
C 30 pts. descent	54.09°N, 42.07°W 54.15°N, 42.14°W 648 – 698 m	9.00 (9.24) 0.01 (0.02) 12:45-46	8.23 0.03 13:33-35	0.77 (1.00) 0.56 (0.49)	−0.02 (−0.007) 0.005 (0.003)
May 27, 2016					
A 166 pts. grazing	54.26°N, 41.31°W 54.06°N, 41.30°W 1384 – 1461 m	9.04 (8.70) 0.04 (0.03) 15:10-12	8.94 0.04 14:39-42	0.01 (−0.24) 0.82 (1.00)	0.005 (−0.009) 0.04 (0.02)
May 30, 2016					
A 11 pts. ascent	44.09°N, 44.43°W 44.11°N, 44.42°W 1539 – 1577 m	10.68 0.10 14:41	11.22 0.10 15:18-19	−0.54 0.99	0.04 0.04
B* 5 pts. descent	44.21°N, 44.36°W 44.22°N, 44.36°W 1635 – 1677 m	*9.40* (13.53) *0.15* (0.02) 14:40	13.51 0.05 15:22	−*4.10* (0.02) *0.63* (0.33)	*0.10* (−0.03) *0.004* (0.01)
C 7 pts. ascent	44.65°N, 44.14°W 44.66°N, 44.14°W 1126 – 1176 m	10.43 0.09 14:34	9.88 0.07 15:29	0.55 1.00	0.02 0.05

for each flight segment, as well as the means and standard deviations of the differences between these parameters from RSP and CDP datasets are presented in Table 1. The results of both RSP retrieval methods are shown with RFT values placed in parentheses.

HSRL depolarization profiles co-located with RSP and CDP data indicate that in some cases at least two separate layers of clouds are present in the scene. In this situation if the top layer is optically thin (optical depth less than one) the RSP retrievals are sensitive to droplet sizes in both layers (see Alexandrov et al. (2012a) for details and simulations). This results in bimodal DSD in RFT retrievals with each size mode associated with its own cloud layer. Alexandrov et al. (2012a) demonstrated that the parametric retrieval algorithm in such case either picks one (dominant) mode (if the other is weak) or fits the whole DSD with a single wide mode having large (0.1 or more) effective variance. The effective radius in the latter case is a weighted average of those in the two modes. While such a wide DSD may be representative of the two-layer system as a whole, it does not reflect microphysics in any one of the layers. Understanding this is especially important for studies of marine Sc clouds which are known to have very narrow DSDs at cloud top (formed as a result of convection) with v_{eff} often smaller than 0.01 (corresponding to about 1 μm standard deviation of radius in DSD) (Alexandrov et al., 2015; Pawlowska et al., 2006). This means that in Sc cases detection of a large v_{eff} should automatically raise suspicion that a multilayer structure is present.

Comparison of RSP retrievals with *in situ* measurements in two-layer situations described above is challenging since the *in situ* DSDs reflect cloud microphysics in a single layer (at a time), and, thus, cannot be directly compared to RSP retrievals representing both layers at once. However, in such cases the RFT can be used to separate DSDs of different layers, one of which can be used for comparison with *in situ* data. In the NAAMES dataset we encountered very wide DSDs in parametric RSP retrievals (corresponding to distinctly bimodal RFT-derived DSDs) in two instances: case A from May 18 and case B from May 30. In the May 18 case two cloud layers are clearly seen in HSRL profiles (Fig. 3). In this case CDP retrievals yield segment-averaged $r_{\rm eff}$ of 10.80 μm and $v_{\rm eff}$ of 0.04, which are quite different from the results of RSP's parametric algorithm: $r_{\rm eff}$ = 5.56 μm and $v_{\rm eff}$ = 0.10. However, the parameters of the larger mode in the RFT-derived distribution ($r_{\rm eff}$ = 10.75 μm and $v_{\rm eff}$ = 0.01) are very close to the *in situ* values. A similar situation is seen in case B from May 30, where the averaged CDP-derived parameters ($r_{\rm eff}$ = 13.51 μm and $v_{\rm eff}$ = 0.05) and those of the larger RFT mode ($r_{\rm eff}$ = 13.53 μm and $v_{\rm eff}$ = 0.02) were close. In contrast the results from the RSP's parametric algorithm were different ($r_{\rm eff}$ = 9.40 μm and $v_{\rm eff}$ = 0.15). The parametric RSP results in both of these cases, being not suitable for comparison with CDP data, are shown in italics in Table 1.

The clouds observed on May 18, 20, and 27 were well-developed stratocumulus with narrow DSDs at cloud tops. In six cases from these days (except case A from May 18 described above) both parametric and RFT retrievals were comparable with *in situ* data. In all of these cases the parameters of the dominant mode in the RFT-derived DSDs were close to those obtained using a parametric fit, being within 0.3 μm in $r_{\rm eff}$ and 0.01 in $v_{\rm eff}$. Table 1 shows that the RSP-CDP biases in $r_{\rm eff}$ for the well-developed Sc cases were mostly positive and within 0.5 μm (except for May 20, C: 0.77–1.00 μm), while the standard deviations were within 0.6 μm (except for May 18, A: 1.50 μm; and May 27, A: 0.82–1.00 μm). The RSP-CDP biases in $v_{\rm eff}$ were mostly negative and no larger than 0.02 in absolute value (except for May 18, A: 0.03), while the standard deviations of $v_{\rm eff}$ in the segments were smaller than 0.01 (except for May 27, A: 0.04).

The subject of our study on May 30 was a cloud with complex structure (probably open-cell Sc) consistent with wide DSDs in both RSP and CDP retrievals ($v_{\rm eff}$ of up to 0.1 on average). Case B for this day was described above as having good agreement between *in situ* parameters and those of one of the RFT-derived size modes. While RFT analysis produced bimodal DSDs also in case C, and especially A, none of the modes showed similarity with CDP-derived size distributions (so we do not show RFT data for these cases in Table 1). Parametric RSP retrievals, on the other hand, showed reasonably good agreement with *in situ* data in both cases: ~ 0.55-μm biases and 1-μm standard deviation for $r_{\rm eff}$, while for $v_{\rm eff}$ biases were below 0.04 and standard deviations – below 0.05. The RSP-CDP comparisons were not expected to be particularly good for this day because the substantial heterogeneity of the cloud field increases spatial and temporal sampling errors. However, the results appear to be quite satisfactory, showing that RSP can provide accurate droplet size retrievals (with accuracy in $r_{\rm eff}$ of 1 μ m, and in $v_{\rm eff}$ – of about 0.04) even for a complex cloud field like this.

The measurement accuracies of cloud DSD parameters required for a reliable quantification of indirect aerosol effect on clouds have been specified by Mishchenko et al. (2004) as being the greater of 1 μm or 10% for $r_{\rm eff}$ and greater of 0.05 or 50% for $v_{\rm eff}$. These requirements are based on the need to detect changes of cloud droplet size caused by increase in cloud condensation nuclei concentrations and to determine the cloud droplet number concentration with at least 30% accuracy. The validation results presented in Table 1 demonstrate that the accuracy of RSP-based retrievals of DSD parameters satsfy and in most cases exceed these requirements.

The validation of polarimetric cloud droplet size retrieval techniques presented in this study demonstrated the value of airborne (and potentially satellite) polarimetric observations and that the resulting retrieved DSDs are robust and accurate. We hope that validation experiments will be continued during future field campaigns and allow for an evaluation of how the information in the remotely sensed DSDs can be used to understand the formation of drizzle at cloud top. Our experience gained during this study will help us to better plan future validation efforts. For example, we recommend that the aircraft should periodically exit cloud when grazing cloud top, so the cloud top height could be determined from *in situ* measurements. Another suggestion is to sample both layers in two-layer cloud structures, thus, alowing for validation of bimodal DSDs.

Acknowledgments

This research was funded by the NASA Radiation Sciences Program managed by Hal Maring and by the NASA ROSES program under Grant NNH13ZDA001N-EVS2. We are tremendously grateful to the NAAMES leadership team that allowed us to obtain such a comprehensive cloud remote sensing dataset. The NASA C-130 pilots, crew and management were immensely supportive and we thank them for all the help they so generously provided. The data used in this study is archived at the NASA Langley Research Center Airborne Science Data for Atmospheric Composition archive at https://www-air.larc.nasa.gov/missions/naames/index.html and is also available at https://data.giss.nasa.gov/pub/rsp/. We would like to thank the NASA Langley Cloud and Radiation Group (https://cloudsgate2.larc.nasa.gov/) for providing the GOES satellite imagery during NAAMES. We also would like to thank A. S. Ackerman for insightful discussions of cloud physics and types, and the two anonymous reviewers for their thoughtful comments that helped us to significantly improve the paper.

Appendix A Droplet size statistics in remote sensing and in situ measurements

Remote sensing and *in situ* measurement communities traditionally use different statistics for characterization of droplet size distributions. While *in situ* measurements commonly report mean droplet diameter, its standard deviation, and relative dispersion, optical remote sensing retrievals are usually expressed in terms of effective radius and variance. For the reference, we present here definitions of these parameters and relationships between them (for uniformity, all statistics is expressed in terms of droplet radius rather than diameter).

Droplet size distribution $n(r)$ has moments

$$\langle r^k \rangle = \int_0^\infty r^k \; n(r) \; \mathrm{d}r \tag{A.1}$$

including the mean radius $\langle r \rangle$. The standard deviation σ is derived from the dispersion

$$\sigma^2 = \int_0^\infty (r - \langle r \rangle)^2 \; n(r) \; \mathrm{d}r = \langle r^2 \rangle - \langle r \rangle^2. \tag{A.2}$$

Another commonly used parameter is relative standard deviation $d = \sigma / \langle r \rangle$ or relative dispersion

$$d^2 = \frac{\sigma^2}{\langle r \rangle^2} = \frac{\langle r^2 \rangle}{\langle r \rangle^2} - 1. \tag{A.3}$$

The optically-driven effective radius and variance are defined as (Hansen & Travis, 1974)

$$r_{\mathrm{eff}} = \frac{\int_0^\infty r \pi r^2 n(r) \mathrm{d}r}{\int_0^\infty \pi r^2 n(r) \mathrm{d}r} = \frac{\langle r^3 \rangle}{\langle r^2 \rangle}, \tag{A.4}$$

and

$$v_{\mathrm{eff}} = \frac{1}{r_{\mathrm{eff}}^2} \frac{\int_0^\infty (r - r_{\mathrm{eff}})^2 \pi r^2 n(r) \mathrm{d}r}{\int_0^\infty \pi r^2 n(r) \mathrm{d}r} = \frac{\langle r^4 \rangle \langle r^2 \rangle}{\langle r^3 \rangle^2} - 1. \tag{A.5}$$

Cloud DSDs often have the gamma distribution shape (Hansen & Travis, 1974):

$$n(r) = \frac{(ab)^{(2b-1)/b}}{\Gamma[(1-2b)/b]} \; r^{(1-3b)/b} e^{-r/ab}, \tag{A.6}$$

where Γ is the gamma function. The parameters $a > 0$, and $b \in (0, 1/2)$ of this distribution coincide with respectively the effective radius and variance:

$$r_{\text{eff}} = a, \quad v_{\text{eff}} = b. \tag{A.7}$$

The mean radius and the standard deviation of gamma distribution are respectively

$$\langle r \rangle = a(1-2b) \;\; \text{and} \;\; \sigma = a\sqrt{b\,(1-2b)}, \tag{A.8}$$

thus, its relative dispersion is

$$d^2 = \frac{b}{1-2b}. \tag{A.9}$$

This allows to express the effective radius and variance of gamma distribution in terms of $\langle r \rangle$ and d:

$$a = \langle r \rangle \; (1+2d^2), \quad b = \frac{d^2}{1+2d^2}. \tag{A.10}$$

For example, typical for Sc clouds values $r_{\text{eff}} = 10$ μm and $v_{\text{eff}} = 0.02$ correspond to $\langle r \rangle = 9.6$ μm, $d = 0.14$, and $\sigma = 1.38$ μm.

Note that the mode radius of gamma distribution is

$$r_{max} = a(1-3b), \tag{A.11}$$

indicating that gamma distribution has maximum only when $b < 1/3$.

References

Alexandrov, M. D., Ackerman, A. S., & Marshak, A. (2010). Cellular statistical models of broken cloud fields. Part II: Comparison with a dynamical model and statistics of diverse ensembles. *J. Atmos. Sci.*, *67*, 2152–2170.

Alexandrov, M. D., Cairns, B., van Diedenhoven, B., Ackerman, A. S., Wasilewski, A. P., McGill, M. J., Yorks, J. E., Hlavka, D. L., Platnick, S. E., & Arnold, G. T. (2016a). Polarized view of supercooled liquid water clouds. *Remote Sens. Environ.*, *181*, 96–110.

Alexandrov, M. D., Cairns, B., Emde, C., Ackerman, A. S., & van Diedenhoven, B. (2012a). Accuracy assessments of cloud droplet size retrievals from polarized reflectance measurements by the research scanning polarimeter. *Remote Sensing of Environment*, *125*, 92–111.

Alexandrov, M. D., Cairns, B., Emde, C., Ackerman, A. S., Ottaviani, M., & Wasilewski, A. P. (2016b). Derivation of cumulus cloud dimensions and shape from the airborne measurements by the Research Scanning Polarimeter. *Remote Sens. Environ.*, *177*, 144–152.

Alexandrov, M. D., Cairns, B., & Mishchenko, M. I. (2012b). Rainbow Fourier transform. *J. Quant. Spectrosc. Radiat. Transfer*, *113*, 2521–2535.

Alexandrov, M. D., Cairns, B., Wasilewski, A. P., Ackerman, A. S., McGille, M. J., Yorks, J. E., Hlavka, D. L., Platnick, S. E., Arnold, G. T., van Diedenhoven, B., Chowdhary, J., Ottaviani, M., & Knobelspiesse, K. D. (2015). Liquid water cloud properties during the Polarimeter Definition Experiment (PODEX). *Remote Sensing of Environment*, *169*, 20–36.

Boucher, O., Randall, D., Artaxo, P., Bretherton, C., Feingold, G., Forster, P., Kerminen, V.-M., Kondo, Y., Liao, H., Lohmann, U., Rasch, P., Satheesh, S., Sherwood, S., Stevens, B., & Zhang, X. (2013). Clouds and aerosols. In T. Stocker, D. Qin, G.-K. Plattner, M. Tignor, S. Allen, J. Boschung, A. Nauels, Y. Xia, V. Bex, & P. Midgley (Eds.), *Climate Change 2013: The Physical Science Basis. Contribution of Working Group I to the Fifth Assessment Report of the Intergovernmental Panel on Climate Change* (pp. 571–657). Cambridge University Press.

Bréon, F. M., & Doutriaux-Boucher, M. (2005). A comparison of cloud droplet radii measured from space. *IEEE Trans. Geosci. Remote Sens.*, *43*, 1796–1805.

Bréon, F.-M., & Goloub, P. (1998). Cloud droplet effective radius from spaceborne polarization measurements. *Geophys. Res. Lett.*, *25*, 1879–1882.

Cairns, B., Russell, E. E., & Travis, L. D. (1999). Research scanning polarimeter: calibration and ground-based measurements. In D. H. Goldstein, & D. B. Chenault (Eds.), *Polarization: Measurement, Analysis, and Remote Sensing* (pp. 186–197). volume 3754 of *Proc. SPIE*.

Deschamps, P. Y., Breon, F. M., Leroy, M., Podaire, A., Bricaud, A., Buriez, J.-C., & Séze, G. (1994). The POLDER mission – Instrument characteristics and scientific objectives. *IEEE Trans. Geosci. Remote Sens.*, *32*, 598–615.

Flato, G., Marotzke, J., Abiodun, B., Braconnot, P., Chou, S., Collins, W., Cox, P., Driouech, F., Emori, S., Eyring, V., Forest, C., Gleckler, P., Guilyardi, E., Jakob, C., Kattsov, V., Reason, C., & Rummukainen, M. (2013). Evaluation of climate models. In T. Stocker, D. Qin, G.-K. Plattner, M. Tignor, S. Allen, J. Boschung, A. Nauels, Y. Xia, V. Bex, & P. Midgley (Eds.), *Climate Change 2013: The Physical Science Basis. Contribution of Working Group I to the Fifth Assessment Report of the Intergovernmental Panel on Climate Change* (pp. 741–866). Cambridge University Press.

Hansen, J. E., & Travis, L. D. (1974). Light scattering in planetary atmospheres. *Space Sci. Rev.*, *16*, 527–610.

Lance, S. (2012). Coincidence errors in a Cloud Droplet Probe (CDP) and a Cloud and Aerosol Spectrometer (CAS), and the improved performance of a modified CDP. *J. Atmos. Oceanic Tech.*, *29*, 1532–1541.

Lance, S., Brock, C. A., Rogers, D., & Gordon, J. A. (2010). Water droplet calibration of the Cloud Droplet Probe (CDP) and in-flight performance in liquid, ice and mixed-phase clouds during ARCPAC. *Atmos. Meas. Tech.*, *3*, 1683–1706.

Mishchenko, M. I. (2006). Glory. In C. L. Parkinson, A. Ward, & M. D. King (Eds.), *Earth Science Reference Handbook: A Guide to NASA's Earth Science Program and Earth Observing Satellite Missions* (pp. 141–147). National Aeronautics and Space Administration.

Mishchenko, M. I., Cairns, B., Hansen, J. E., Travis, L. D., Burg, R., Kaufman, Y. J., Martins, J. V., & Shettle, E. P. (2004). Monitoring of aerosol forcing of climate from space: analysis of measurement requirements. *J. Quant. Spectrosc. Radiat. Transfer*, *88*, 149–161.

Mishchenko, M. I., Cairns, B., Kopp, G., Schueler, C. F., Fafaul, B. A., Hansen, J. E., Hooker, R. J., Itchkawich, T., Maring, H. B., & Travis, L. D. (2007). Accurate monitoring of terrestrial aerosols and total solar irradiance: Introducing the Glory mission. *Bull. Amer. Meteorol. Soc.*, *88*, 677–691.

Mishchenko, M. I., Travis, L. D., & Lacis, A. A. (2006). *Multiple Scattering of Light by Particles: Radiative Transfer and Coherent Backscattering*. Cambridge University Press.

Pawlowska, H., Grabowski, W. W., & Brenguier, J.-L. (2006). Observations of the width of cloud droplet spectra in stratocumulus. *Geophys. Res. Lett.*, *3333, L19810*.

Platnick, S. (2000). Vertical photon transport in cloud remote sensing problems. *J. Geophys. Res.*, *105*, 22919–22935.

Rogers, R. R., & Yau, M. K. (1989). *A Short Course in Cloud Physics*. (3rd ed.). Pergamon Press.

Waquet, F., Cairns, B., Knobelspiesse, K., Chowdhary, J., Travis, L. D., Schmid, B., & Mishchenko, M. I. (2009). Polarimetric remote sensing of aerosols over land. *J. Geophys. Res.*, *114, D01206*.

List of Figure Captions

Figure 1. CDP-derived vertical profiles of droplet effective radius (left) and variance (right) for May 18, 2016 (see Fig. 3 for the location and CDP altitude). Linear fits are provided to show how fast these parameters change with altitude near cloud top.

Figure 2. GOES satellite image of North Atlantic ocean for 11:15 UTC on May 18, 2016. The coastline of Newfoundland is shown in the West, while that of Greenland – in the North. The vicinity of the validation flight segments is depicted by red circle.

Figure 3. HSRL depolarization ratio profile for the May 18 case. Black curve depicts the altitude of the aircraft during the *in situ* segment. Red points on this curve indicate availability of CDP measurements with $r_{\text{eff}} > 4.5\ \mu$m. The pairs of vertical green lines labeled A and B indicate the intervals used for RSP-CDP intercomparisons presented in Table 1. The DSDs from the top points of these intervals are shown in Fig. 5.

Figure 4. Top and middle: effective radius and variance, respectively, retrieved from the RSP data using the parametric fitting technique (blue curves). The discretization seen in these plots is that of the LUTs used. Bottom: the results of mode decomposition applied to distributions derived from RSP data using RFT. The curves depicting the modes' effective radii are colored according to the modes' respective weights in DSD. The red curves in all panels depict the screened co-located CDP retrievals. The pairs of vertical green lines labeled A and B indicate the intervals used for RSP-CDP intercomparisons presented in Table 1.

Figure 5. RSP- (blue) and CDP-derived (red) droplet number (left) and

area (right) distributions corresponding to cloud exit (A: 11.98 h UTC, top) and entrance (B: 12:03 h UTC, bottom) in the May 18 case (see Fig. 3). The presented RSP retrievals are parametric in left plots and RFT-derived in right plots.

Figure 6. Same as Fig. 2 but for 12:45 UTC on May 20, 2016.

Figure 7. Same as in Fig. 3 but for May 20, 2016 case. The pairs of vertical green lines labeled A, B, and C indicate the intervals used for RSP-CDP intercomparisons presented in Table 1. The DSDs from the top points of these intervals are shown in Fig. 9.

Figure 8. Same as in Fig. 4 but for May 20, 2016 case. The pairs of vertical green lines labeled A, B, and C indicate the intervals used for RSP-CDP intercomparisons presented in Table 1.

Figure 9. RSP- (blue) and CDP-derived (red) droplet radius (left) and area (right) distributions corresponding to cloud top (A: 13.40 h UTC, top); exit (B: 13.52 h UTC, middle); and entrance (C: 13.56 h UTC, bottom) in the May 20 case (see Fig. 7). The presented RSP retrievals are parametric in left plots and RFT-derived in right plots.

Figure 10. Same as Fig. 2 but for 15:15 UTC on May 27, 2016.

Figure 11. Same as in Fig. 3 but for May 27, 2016 case. Two solid vertical green lines bound the single interval (A) used for comparisons. This two lines together with dashed line between them represent points used in DSD shape comparisons shown in Fig. 13.

Figure 12. Same as in Fig. 4 but for May 27, 2016 case. Two solid green lines bounding the comparison interval and dashed line between them represent points used in DSD shape comparisons shown in Fig. 13.

Figure 13. RSP- (blue) and CDP-derived (red) droplet radius (left) and area (right) distributions selected from May 27 data. The CDP time stamps for these examples are 14.70 h UTC (top), 14.68 h UTC (middle), and 14.65 h UTC (bottom). The presented RSP retrievals are parametric in left plots and RFT-derived in right plots. The top and bottom plots correspond to the ends of the comparison interval (solid green lines in Figs. 11 and 12), while the middle plots show distinctly bimodal DSD from the middle of the interval (depicted by dashed line in Figs. 11 and 12).

Figure 14. Same as Fig. 2 but for 14:45 UTC on May 30, 2016.

Figure 15. Same as in Fig. 3 but for May 30, 2016 case. The pairs of vertical green lines labeled A, B, and C indicate the intervals used for RSP-CDP intercomparisons presented in Table 1. The DSDs from the top points of these intervals are shown in Fig. 17.

Figure 16. Same as in Fig. 4 but for May 30, 2016 case. The pairs of vertical green lines labeled A, B, and C indicate the intervals used for RSP-CDP intercomparisons presented in Table 1.

Figure 17. RSP- (blue) and CDP-derived (red) droplet radius (left) and area (right) distributions corresponding to the aircraft exiting the cloud top (A: 15.31 h UTC, top); entering the cloud from above (B: 15.34 h UTC, middle); and crossing a thin part of the cloud (C: 15.48 h UTC, bottom) in the May 30 case (see Fig. 15). The presented RSP retrievals are parametric in left plots and RFT-derived in right plots.